Flow, mixing and heat transfer in fluidic oscillators

Document Version:
Peer reviewed version

Flow, mixing and heat transfer in fluidic oscillators

Chirag M. Khalde,[a] Ajinkya V. Pandit,[b] Jitendra S. Sangwai,[a] Vivek V. Ranade[c,*]

[a]Gas Hydrate and Flow Assurance Laboratory, Petroleum Engineering Program,
Department of Ocean Engineering, Indian Institute of Technology Madras,
Chennai 600036, India.

[b]Chemical Engineering and Process Development Division,
CSIR - National Chemical Laboratory,
Pune 411008, INDIA

[c]Multiphase Flows, Reactors and Intensification Group (mRIg)
School of Chemistry and Chemical Engineering,
Queen's University Belfast,
Belfast BT9 5AG, Northern Ireland, UK

*Corresponding Author:
Vivek V. Ranade: V.Ranade@qub.ac.uk

Abstract

There is an increasing emphasize on process intensification and development of compact, intensified reactors and separators in recent years. Significant efforts are being made to develop such intensified reactors and separators without any moving parts. Few of the recent research studies have proved that liquid – liquid extractor based on the Coanda effect and feedback oscillations exhibit excellent mixing and liquid – liquid contacting. These fluidic oscillators can potentially be used for variety of other multiphase reactions and systems demanding enhanced mixing, heat and mass transfer. In this work, we have computationally investigated flow, mixing and heat transfer in fluidic oscillators based on the Coanda effect. Available information on flow and mixing in fluidic oscillators was critically reviewed and key gaps in the available knowledge with respect to design and optimization of fluidic oscillators were identified. Computational flow models were developed to characterize key flow features like unsteady flows, secondary vortices and internal recirculation over a range of Reynolds number ($Re = 90$ to 1538) for three different oscillator designs. Systematic numerical studies were carried out to quantify different flow regimes, oscillations and influence of key geometric parameters on flow, mixing and heat transfer. Simulated results were critically analyzed and are presented in the form of dimensionless numbers. The approach and results presented in this work will provide useful insights and a systematic basis for extending the applications of the Coanda based feedback oscillatory devices for a wide range of engineering applications.

1. Introduction

Intensified reactors and separators without any moving parts owing to variety of advantages are finding increasing applications in chemical and pharmaceutical industries (Hessel et al., 2004)[1]. These devices offer various advantages like easy maintenance and service, simple for fabrication and flow/reaction control. A variety of innovative designs have been developed based on different principles to generate/initiate an oscillatory flow of fluids. For examples, resonating cavity (Campagnuolo and Lee, 1969)[2] pressure based oscillator working on the principle of inductance-resistance feedback loop (Campagnuolo and Gehman, 1968)[3] pneumatic oscillator (Pichini, 1967)[4] etc. One type of the fluidic oscillator which has interconnection channels and works on feedback mechanism was first developed by Spyropoulos (1964).[5] These oscillators use Coanda effect in which a jet flow attaches itself to a nearby flat or curved surface. These oscillators are being used for variety of applications, be it employed as an actuators and flow meters (Tippet et al., 1973[6]; Wright, 1980[7]; Shakouchi, 1989[8]; Tesař et al., 2006[9]; Yang et al. 2007[10]), liquid-liquid extractor (Wang and Xu, 2014)[11] chemical/biochemical reactor (Xu and Chu, 2014)[12] water treatment (Rehman et al., 2015)[13] separation controlling devices (Schmidt et al. 2017)[14] drug or explosives detector or microfluidic droplet generators (Beatus et al., 2012; Xu and Dai, 2015)[15,16].
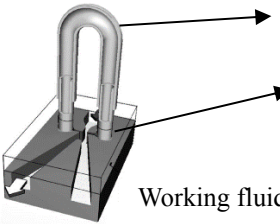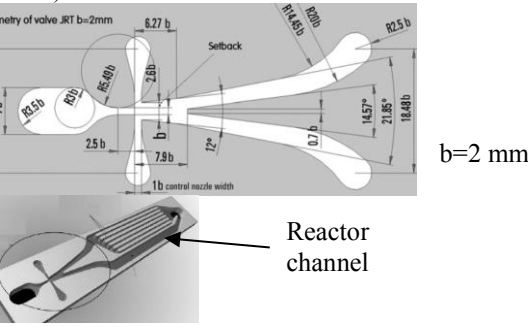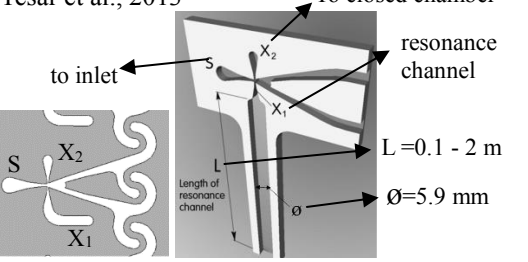
There is a renewed interest in these oscillators in recent years with the advent of micro-fluidics and intensified continuous processes for fine and specialty chemicals. These recent works replaced the control loop used in early studies by two feedback channels. These feedback oscillators showed promising mixing characteristics over a wide range of flow rates (Reynolds numbers). Significant efforts have been invested for the development, and improvements in the design of these fluidic oscillators. Recent progress on the state-of-the-art fluidic oscillators having feedback loop mechanism is briefly reviewed by Xu and Xie (2017)[17] for liquid-liquid extractions and by Gregory and Tomac (2013)[18] for actuator or sensor applications. Some of the key studies on the feedback loop fluidic oscillators are summarized in Table 1. Review of published information indicates that the geometric parameters like the jet width, chamber height, limb height, limb location, etc., are the critical parameters which govern the jet oscillations. In these devices, the formed secondary vortices play a crucial role in the jet switching mechanism and thereby the mixing (Krüger et al., 2013)[19]. McDonough et al. (2017)[20] have reported results on the influence of seven geometrical parameters on the flow-switching frequencies produced in 3D printed single feedback loop. They observed that the most consequential parameter controlling oscillations was the splitter distance (distance between the power nozzle and two outlet streams). The angle between the outlet channels was also found to be important, with wider angles producing slightly higher frequencies. Lower inlet zone length and wider feedback loops were found to inhibit flow switching. From liquid-liquid extraction perspective, Xu and coworkers have contributed many such innovative designs. However, any attempts to further
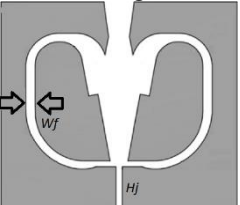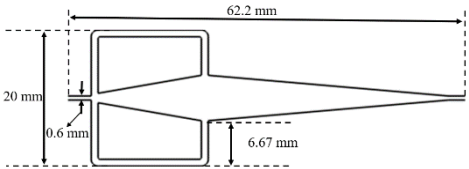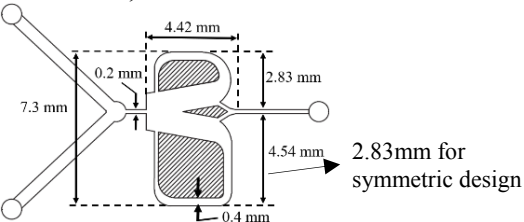
enhance the design effectiveness by fundamentally studying the flow features, is missing (Xu and Meng, 2013)[21]. It is essential to compare different designs and quantify influence of key design and operating parameters on flow, mixing, residence time distributions and heat transfer so that useful guidelines necessary for expanding applications of these devices may be developed. Internal circulation through feed-back arms offer new opportunities to control residence time distribution of dispersed phase in such oscillators and therefore may open up many new ideas and applications[16]. However, adequate understanding and quantitative information on internal recirculation and subsequent interactions with flow oscillations – mixing – heat transfer is lacking. In this work, we have attempted to fill some of these gaps by carrying out detailed computational investigations to characterize key flow features like unsteady flows, secondary vortices and internal recirculation within such fluidic oscillators.
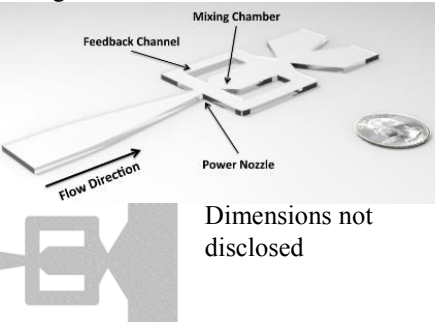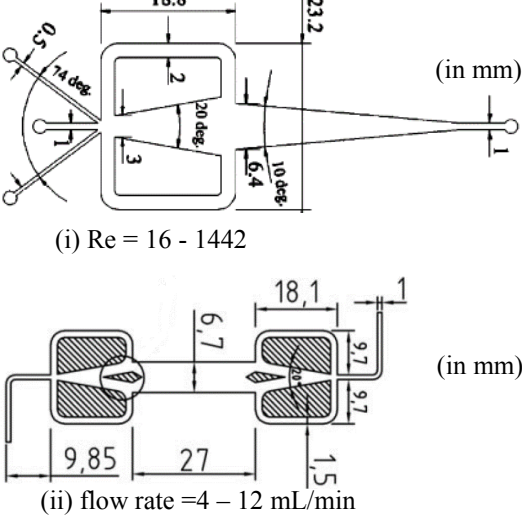
When a free stream jet flows through a nozzle into a chamber, the jet has a tendency to get attached to the neighboring wall of the chamber which is known as Coanda effect[22]. Desired flow, mixing and heat transfer in fluidic oscillator is mainly realized due to the Coanda effect, jet instability, and the alternating mass flow/pressure variation across limbs. These factors are primarily dependent on the relative dimensions of chamber width, feedback loop width and jet width for a fluidic oscillator. In this work, since the objective is to develop quantitative understanding of flow, mixing and heat transfer in devices suitable for variety of applications (not just micro-fluidics), we have selected two different design configurations: one proposed by Wang and Xu (2014)[11] and the other proposed by Xie and Xu (2017)[23]. The previous studies have pointed out some of the lacunae in these designs. For example: both these designs indicate ineffective utilization of energy content of the generated vortices to mixing. Maximum mixing intensity is reported as 75% by Xie and Xu (2017)[23] which indicate potential for further improvements. The configuration used by Xie and Xu (2017)[23] generates dead zones (KAM tori region [will be discussed later]) making it unsuitable for certain applications. Obstruction or deflector used in their device may suppress vortex growth and thereby reduce mixing effectiveness. The extractor developed by Wang and Xu (2014)[11] has an inherent advantage of not having any dead zones, but has a reduced volumetric capacity. Based on this analysis, in addition to these two configurations, we also have considered a third design of oscillator with increased width of the mixing chamber and reduced limb lengths. The three configurations considered in this work are shown in Figure 1.

In this work, flow, mixing and heat transfer characteristics of three different oscillator designs shown in Figure 1 over a range of Reynolds number (*Re* = 90 to 1538) are presented. The approach and results presented in this work will provide useful insights and a systematic basis for extending the applications of the Coanda based feedback oscillatory devices for a wide range engineering application.

4
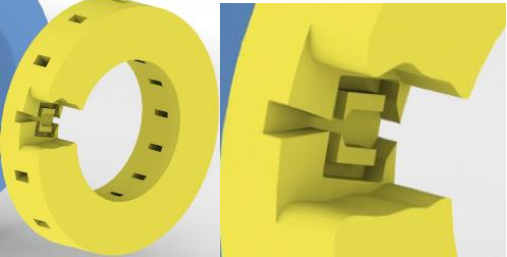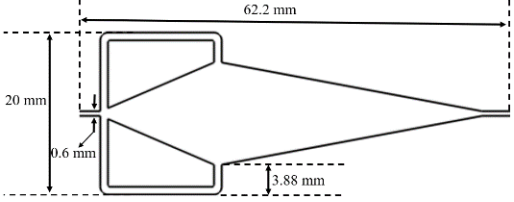
Table 1: Brief review of recent studies on fluidic oscillators

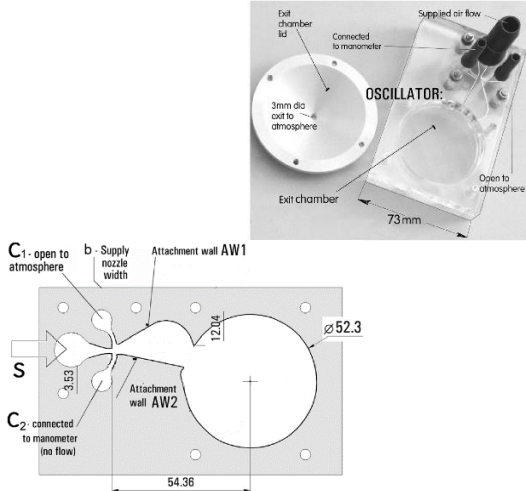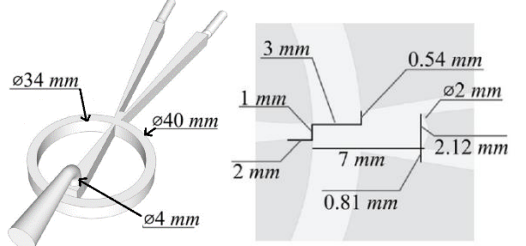| Literature and design details	Applications	computational /experimental/analytical details	Comment
Tesař et al., 2006[9] Loop: Diameter: 2.5-10mm Length: 1 to 100 m Inlet nozzle: 0.5 mm Working fluid: air Re=1790-14340	Oscillating flow amplifier	Experimental study: Devices/methodology/measured parameters: • external excitation using amplifiers, • piezometric pressure transducer; • frequency	• Wide operating range achieved by modification of loop length and loop diameter • Experimental verification of lab scale model to generate hybrid synthetic jets • Oscillating frequency inversely proportional to the length of feedback loops • Detailed analysis of loop diameter influence of jet oscillation: loop flow rate, frequency, resonance, etc.
Tesař, 2009[24]; (working concept in Tesař, 2001)[25] b=2 mm Reactor channel Working fluid: air; Re=10300	automobile exhaust system, uniform flow distribution reactor	Computational Study: • 2D simulations • grid size: 30,000 • turbulence model: RNG RANSE; • Measured parameters: pressure drop; path lines; mass flow rate	• Developed a fluidic oscillator design consisting of fluidic bi-stable diverter valves. • Detailed study of Coanda effect and indirect feedback mechanism (using temperature/pressure sensors) • Controlled flow rate through the reactor channel, thereby maintaining uniformity in the mass flow rate/pressure drop.
Tesař et al., 2013[26] To closed chamber resonance channel to inlet L =0.1 - 2 m Ø=5.9 mm Working fluid: air; Re = 5000-30000	Flow separation controller; amplifier	Experimental study: • 7 oscillators strategically connected in series • Excitation using resonance tube of varying length • Measured quantities: flow rate, frequency,	• Proposed a new oscillator which generates jet oscillations by controlling the acoustic waves in the open ended tubes. • Array of such modified oscillators when strategically connected were found to produce wide range of oscillation frequency independent of flow rates.

			temperature; Mass flow rate	• The quarter-wave resonance tube length dictates the oscillating frequency. The acoustic waves cause phase-delayed switching of the amplifier.
Xu and Meng, 2013[21] Hj = 2-8 mm Wf = 4.8-8 mm width =6-16 mm length×breadth = 330 mm ×90 mm Working fluid: water; Re = 8000-50000	Flow meter	Experimental study and analytical study • Instruments: Ultrasonic flow meter; pressure transmitter • Measures quantities: Pressure response, frequency	• Geometric characterization of symmetric loop oscillator • Developed an empirical performance characteristic curve for frequency as a function of Reynolds number, limb width, nozzle diameter and chamber dimensions.	
Wang and Xu, 2014[11] 62.2 mm 20 mm 0.6 mm 6.67 mm Working fluid: tributyl phosphate-kerosene and 3M HNO$_3$ solutions; Re = 256-1282 (based on inlet hydraulic diameter)	co-current Liquid-liquid extractor	Experimental study: • Flow visualization techniques used for the study • Instruments: Stereoscopic microscope; High speed camera, flowmeter; Inductively coupled plasma for concentration Measurement	• Successfully dispersed aqueous phase liquid into small droplets using the symmetric oscillator. • Extraction efficiency increases with increase in flow rates. • 90% extraction efficiency.	
Xu and Chu, 2014[12] 4.42 mm 0.2 mm 2.83 mm 7.3 mm 4.54 mm 2.83mm for symmetric design 0.4 mm Working fluid: tributyl phosphate-kerosene and 3M HNO$_3$ solutions; Re = 100-606 (based on inlet hydraulic diameter)	Liquid-liquid extractor	Experimental study: • Flow visualization techniques used for deciphering flow physics • Instruments: Stereoscopic microscope; High speed camera, ICP for concentration Measurement	• A new design with an obstruction placed in the mixing chamber • Amplification of unbalanced forces observed in asymmetric design compared to symmetric design. • Extraction efficiency is higher for asymmetric design compared to symmetric at all *Re*. • Extraction efficiency improves from 94% to 97% due to asymmetry.	

Bobusch et al., 2013;[27] Woszidlo et al., 2015; [28] ; Kruger et al. 2013[19]	Flow control actuators	Computational Study:	• A fundamental study has been carried for studying the transient jet behavior within and outside the mixing chamber.
 Dimensions not disclosed Working Fluid: Water; *Re* = 16034		• Grid size = 0.55 million (2D); 2.8 million (3D) (unstructured grids) • Turbulence model: *k-ε*, *kω-SST* Experimental study • Details: PIV, Pressure, mass flow rates and temperature measurements devices	• Jet undergoes sinusoidal oscillations outside the mixing chamber due to the alternate switching of the flow by the feedback loop. • Increase in the formed separation bubble size is primary factor for switching of the flow. • A detailed optimization study done for the investigated oscillator geometry to suit the requirements of certain applications.
(i) Xu and Dai, 2015[16] ; (ii) Xu et al., 2016[29] (i) Re = 16 - 1442 (ii) flow rate =4 – 12 mL/min Working fluid: HNO₃ solution and fully hydrogenated kerosene with 0.3 wt % Span 80 surfactant	Droplet generator and extractor	Experimental study • Flow visualization techniques used for the study • Instruments: Stereoscopic microscope; High speed camera, flowmeter; Inductively coupled plasma for concentration Measurement	The symmetric fluidic oscillator has been successfully used to produce droplets of two immiscible liquids with a high throughput. It was found to be very suitable for solvent extraction and other chemical processes that require a high surface/volume ratio. Xu and Dai, 2015[16] • The device with feedback channels has good extraction capabilities compared to the case without feedback channels. • Reduction in the wetting of walls by the aqueous phase due to the presence of surfactants improved the performance of extraction. Xu et al., 2016[29] • A systematic process of utilization and operations of the novel extractor design with feedback loops has been presented for droplet generation and extraction. The developed methodology was successfully incorporated using pulsed feeding mechanism

Tesař, 2015[30] Working Fluid: air; Re = 2000 – 12000	Sensor	Experimental study: Device/measured parameters/methodology: • Pressure gauges, manometers used for pressure drop measurement; frequency and power spectral density response for acoustics	• A sensor has been developed and characterized for high value of Reynolds number • Three regimes have been observed based on the Strouhal number variation with *Re* • linear increment in frequency observed from Re = 2000 to 6000 defined as primary region; Transition region from 6000 to 9000; resonance region indicating constant frequency from 9000 to 14000 • Device capable of generating oscillations in the kilohertz range (1.8 to 8.2kHz)
McDonough et al., 2017[20] Working fluid: glycerol–water mixtures; Re ≈ 10^2 -10^4	Liquid extractor	Experimental study: • 3D printed fluidic oscillators of different geometrical designs • oscilloscope; pressure transducer; gear pump	• An experimental study was conducted on 3D-printed oscillators for its characterizations. • Effect of viscosity and flow rate variation on the jet dynamics have been discussed along with the driving mechanism for flow switching/oscillations of the jet. • Optimization study using following parameters: Dimensions and orientation of the feedback loop, splitter distance, nozzle convergence length, inlet zone length and outlet channel angle.
Bobusch et al., 2015[31]	Injector in modern low emission combustion systems	Experimental study: Reported/ instruments/parameters: • 4 different types of injectors studied, viz., slit, rectangular circular and fluidic oscillator.	• Fluidic oscillators have been first employed in standard jet in crossflow fuel injection configurations. • Mixing does not depend much on the flow rates as in the case of standard injectors.

Hydraulic diameter = 1.31 -2.87 mm Jet outlet area = 12-28 mm^2 Working fluid: Water; Re = 7223 – 8092; cross flow momentum =1.3 – 62.5		• High speed camera; laser optics; Planar Laser Induced Fluorenscence • Instantaneous flow properties, concentration, cross flow momentum	• High quality mixing of air fuel mixture can be obtained in a shockless explosion combustion process. • Primary requirement of SEC that flow rates independent of cross flow momentum is easily satisfied by oscillator injectors.
Present work Working Fluid: water; Re =91 - 1538	Chemical reactor; Liquid extractor; mixer	Computational study: • 2D simulations on three different designs • grid size: 0.4-0.6 million (structured grid) • Single phase, multispecies, laminar flow with heat transfer • Reported: non-dimensional fluctuating kinetic energy; mixing intensity, energy dissipation, heat transfer, dispersion number; limb/inlet flow ratio	• A computational comparative study of different designs well established for liquid-liquid extraction process. • Effect of flow, heat transfer, mixing and RTD • The limb effect, chamber width effect and the fundamental working principle of fluidic oscillators have been studied. • WS design (increased chamber width and reduced limb height) is found to perform better than other designs in all the considered aspects and applications.

(i) WS (Present design) (ii) SL (Wang and Xu, 2014)[11] (iii) OD (Xie and Xu, 2017)[17]
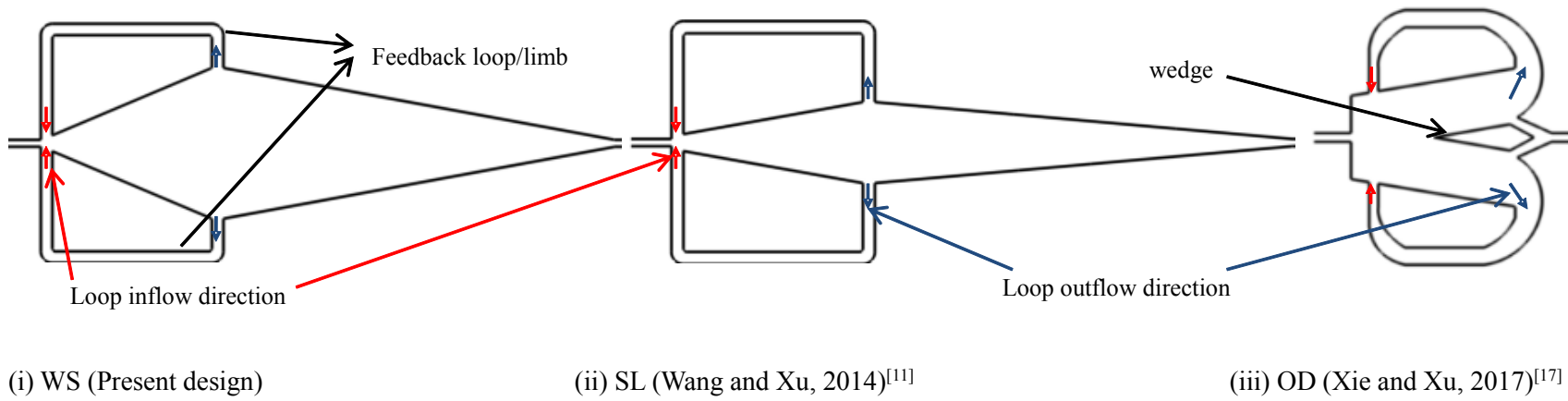
(a): Schematic diagram of the geometries studied in this work

(b) Schematic diagram of feedback loop passive mixer indicating the boundary conditions and critical dimensions.
(● = monitor point at x= 3.4 mm; y = 0 from central axis
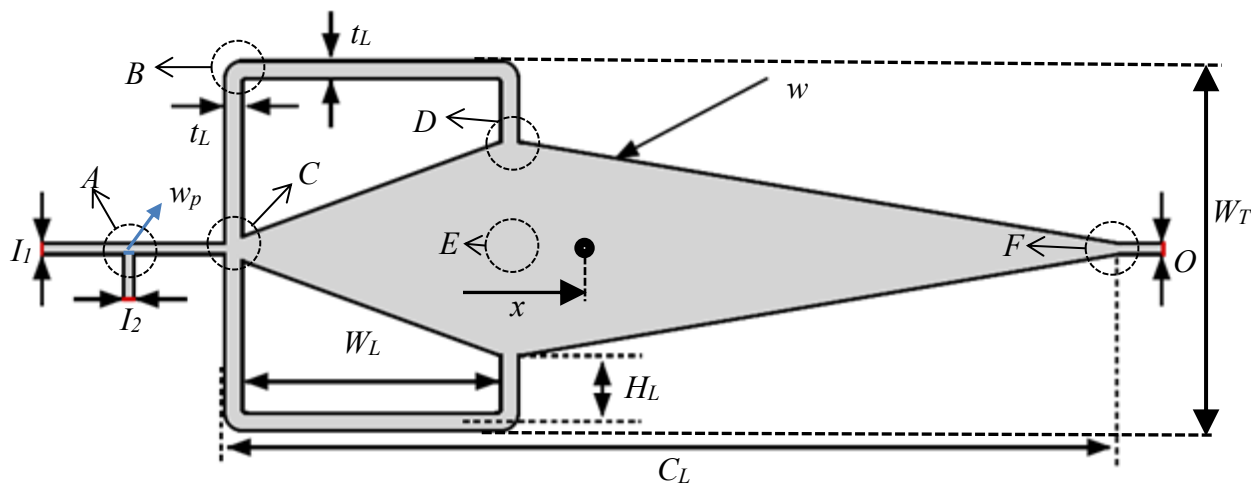
Figure 1: Geometries of fluidic oscillators investigated in this work

2. Computational Model

In the feedback loop oscillators, the interaction between flow through the feedback loops and the oscillating jet establishes a complex oscillating flow within the domain consisting of secondary vortices and separation bubble (Bobusch et al. 2013)[27]. It is therefore essential to model unsteady flow processes. The considered designs and operating conditions indicate laminar flow. The generation, interaction, shedding, splitting, and merging of vortices within considered fluidic oscillators is simulated by solving transient Navier-Stokes equations. The model equations, boundary conditions, post-processing methodology and details of numerical solution are discussed in the following.

2.1 Model equations

The following governing equations, viz., continuity, momentum and energy balance equations were solved for simulating the flow and heat transfer in the selected geometries (Ranade, 2001)[32]:

$$\nabla \cdot \mathbf{u} = 0 \tag{1}$$

$$\frac{\partial \mathbf{u}}{\partial t} + (\mathbf{u} \cdot \nabla)\mathbf{u} = \frac{1}{\rho}\nabla P + \vartheta\nabla^2\mathbf{u} \tag{2}$$

$$\frac{\partial E}{\partial t} + \nabla \cdot \left[\mathbf{u}\left(E + \frac{P}{\rho}\right)\right](\nabla)\mathbf{u} = \frac{\nabla}{\rho}[k\nabla\mathrm{T} + (\bar{\bar{\tau}} \cdot \mathbf{u})] \tag{3}$$

where, $\mathbf{u}$ is the velocity vector (m/s), ρ is the density of the fluid (kg/m^3), P is the pressure (N/m^2), t is the time (s), ϑ is the kinematic viscosity of the fluid (m^2/s), E is the total energy per unit mass (Nm/kg), T is the temperature (K) and $\bar{\bar{\tau}}$ is the viscous dissipation or the stress tensor (N/m^2).

For simulating mixing and residence time distribution, following species transport equation was used for carrying out multispecies flow in the three selected designs (Ranade, 2001)[32]:

$$\frac{\partial(\rho m_k)}{\partial t} + (\mathbf{u} \cdot \nabla)m_{km} = D_{km}\nabla^2 m_k \tag{4}$$

where, m_k is the mass fraction of the tracer of species k and D_{km} is the mass diffusion coefficient of species k in the mixture. The density and kinematic viscosity of the fluid and mass diffusivity of tracer in mixture were considered as constant.

2.2 Configurations of oscillators and boundary conditions

Flow, mixing and heat transfer simulations were carried out on all the three selected geometries (shown in Figure 1a) for a range of *Reynolds* number. The dimensions of the geometrical configurations of WS and SL are listed in Table 2. The length of mixing chamber for WS and SL was 51.33 mm (61.2 mm considering extended inlet/outlet connectors). Total width for WS and SL designs i.e. from extreme end of top limb to bottom limb is 21 mm and 20 mm respectively. Maximum width of the mixing chamber is 13.24 mm for WS design and 6.67 mm for SL design. Geometric details of configuration OD were same as those reported by Xie and Xu (2017)[23] and have not been repeated here.

Table 2: Geometry details and boundary conditions

Line/ Surface	Dimensions (mm)		Boundary conditions
	WS	SL	
I_1, I_2	0.6	0.6	Velocity inlet
O	0.6	0.6	Periodic surfaces; mass flow rate, bulk inlet temperature (300 K) (for periodic simulation)
w_p	0.6	0.6	Wall with no slip; constant wall temperature (340 K) for periodic simulation; interior, when both inlets activated
O	0.6	0.6	Pressure outlet
W	-	-	Wall with no slip; constant wall temperature (340 K)
W_L	14.83	14.83	-
C_L	51.33	51.33	-
H_L	3.88	6.67	
W_T	21	20	
T	1	1	-
Other parameters			
D_H	0.923 mm	0.923 mm	Hydraulic diameter
Volume	823 mm^3	517 mm^3	-
W	2 mm	2 mm	assumed depth of the oscillator

Note: Geometric details of OD are given in Xie and Xu (2017)[23].

For transient simulations carried out in this work, two inlets denoted as I_1 and I_2 were defined as velocity inlet whereas w_p is defined as interior as shown in Figure 1b. The outlet, O is defined as pressure outlet (constant pressure boundary). Reynolds number is calculated using the mean outlet velocity and hydraulic diameter (D_H). For WS and SL geometries, simulations were carried out at superficial velocities (based on outlet) of 0.139, 0.278, 0.556, 0.833, 1.111, 1.389 and 1.667 *m/s*. The simulations for the OD geometry were carried out at superficial velocities of 0.25, 0.5, 1, 1.75 and 2.5 *m/s*. Preliminary simulations were carried out in 3D configurations. These simulations indicated that the depth of the oscillator has diminishing impact on the flow characteristics with increase in thickness. In order to keep the demands on computational resources to manageable level, all the simulations in this work were carried out assuming two-dimensional

configurations. The influence of depth will be considered separately for the optimal configuration obtained from the 2D simulations for future studies.

For heat transfer studies, the considered configuration were taken as a periodic unit: the velocity inlet I_1 was changed to interface such that I_1 and O are defined as periodic surfaces. I_2 region was made inactive (defined as wall). All the solid walls were defined as isothermal walls having constant temperature of 340 K, whereas the bulk fluid was assumed to be entering the oscillator at a temperature of 300 K. Mass flow rates were defined for the periodic surfaces based on the inlet velocities considered for flow simulations. Coupled flow and heat transfer simulations were performed for the three selected geometries. Mixing studies were carried out by splitting the inlet I_1 into two parts for allowing water and tracer (having fluid properties same as water) to flow into the oscillator from each half of the inlet. The surface w_p is defined as wall and I_2 was inactive. Therefore, the streams of water and tracers observe a straight channel from I_1 up to mixing chamber without presence of any T-junction. A self-explanatory schematic has been shown in Figure S1c of SI for the boundary conditions used for this study. This strategy of modification in the boundary conditions was done to isolate mixing characteristics of oscillator from that of T junction. These boundary conditions will ensure capturing of mixing effects owing to the oscillator design alone.   The simulations of residence time distribution (RTD) were carried out for the WS geometry at different Re. Boundary conditions as used for studying flow behavior were used (two inlets I_1 and I_2 were defined as velocity inlet, w_p was defined as interior and O was defined as pressure outlet). The velocity through both the inlets was set to equal values such that the total mass flow rates through outlet were same as corresponding to flow and heat transfer simulations. The statistically converged case from flow simulations was used as an initial condition for these simulations. Tracer (having same properties as water) was injected for 0.02τ seconds (where τ is a ratio of oscillator volume to volume flow rate through the oscillator, $\tau = V_R/q$). After the pulse, the tracer mass fraction was set to zero at the I_2.

Water was used as the working fluid of constant density (ρ) of 1000 kg/m^3, dynamic viscosity (μ) of 0.001 $kg/m.s$ and thermal conductivity of 0.6 $W/m.K$. For mixing and RTD studies, the defined secondary fluid tracer was assumed to have same properties as that of water with mass diffusivity (D_{km}) of 2×10^{-9} m^2/s.

2.3 Key dimensionless parameters and post processing of results

The key non-dimensional parameters for simulation for flow: Reynolds number (Re), Strouhal number (St) and frictional factor (f) are defined as:

$$Re = \frac{\rho u D_H}{\mu}; \quad \text{where} \quad D_H = \frac{4A_{jet}}{P_i} \tag{5}$$

$$St = \frac{fD_H}{u} \tag{6}$$

$$\frac{dP}{L} = \frac{2f\rho u^2}{D_H} = \left[\frac{N}{m^3}\right] \tag{7}$$

where, μ is the dynamic viscosity (kg/ms), D_H is the hydraulic diameter (m) based on the inlet jet area and its perimeter. $P_i(m)$ is the perimeter of the jet at the inlet of the mixing chamber, $A_{jet}(m^2)$ is the cross-sectional area of the jet at the inlet and L (m) is the total length of the unit oscillator. The depth (w) of the oscillator geometry was assumed to be 2 mm while calculating the hydraulic diameter.

For characterizing oscillatory flow, a new key parameter: non-dimensional fluctuating kinetic energy (ξ), is defined as:

$$\xi = \frac{fluctuation\ kinetic\ energy}{volumetric\ mean\ kinetic\ energy} = \frac{\frac{1}{2}\left((\dot{v}_x)^2 + (\dot{v}_y)^2\right)_i}{\frac{1}{V_R}\int \frac{1}{2}\left((\bar{v}_x)^2 + (\bar{v}_y)^2\right)dV} \tag{8}$$

where, $\dot{v}_x, \dot{v}_y$ are the mean velocity fluctuations in x and y direction. $\bar{v}_x, \bar{v}_y$ are the mean velocity components in x and y direction and V_R is the volume of the single unit of the selected oscillator.

Parameters for accounting the dissipation of the energy are:

$$\varepsilon = \frac{dP \times q}{m} = \left[\frac{m^2}{s^3}\right] \tag{9}$$

where, ε is the energy dissipation rate per unit mass and m is the mass of liquid contained in the oscillator. Please see Supplementary Information for the geometry having two inlets and one outlet.[33]

The Nusselt number (Nu) was calculated as:

$$\dot{Q}_{in} = \dot{m}C_P(T_{in} - T_{out}) = h_{avg}A_w\Delta T_{LMTD} \tag{10}$$

$$\Delta T_{LMTD} = \frac{(T_{in} - T_{out})}{ln\left(\frac{T_w - T_{in}}{T_w - T_{out}}\right)} \tag{11}$$

$$Nu = \frac{h_{avg}D_H}{k} \tag{12}$$

Where, $\dot{Q}_{in}$ is the heat input to fluid through the wall, $\dot{m}$ is the mass flow rate of the fluid, C_P is the specific heat at constant pressure of the fluid, A_w is heated wall area, ΔT_{LMTD} is mean logarithmic temperature difference, h_{avg} is convective heat transfer coefficient, T_w is the wall temperature, T_{in} and T_{out} are inlet and outlet temperatures.

Mixing realized within the oscillator/reactor was quantified by evaluating mixing intensity (I_M). The mixing intensity based on the obtained time history of the mass tracer at the outlet was defined as:

$$I_M = 1 - \sqrt{\frac{s^2}{s_{max}^2}} \text{ where } s^2 = \frac{1}{|A|} \int_A (m_k - \overline{m}) \, dA \tag{13}$$

where s is the variance, A is the area of the selected monitored surface (outlet) and $\overline{m}$ is the average mass fraction of the reference surface (inlet).

For RTD studies, simulated tracer concentration/mass fraction profiles for each selected Re were analyzed using classical dispersion model (Levenspiel, 2012)[34]. The mean average residence time ($\bar{t}$), variance of the curve (σ^2), $E - \theta$ curve, and Dispersion number $\left(D = \frac{\Gamma}{uL}\right)$ (where, Γ is the dispersion coefficient), were calculated as:

$$\bar{t} = \frac{\int_0^\infty tC dt}{\int_0^\infty C dt} = \frac{\sum_i t_i \bar{C}_i \Delta t_i}{\sum_i \bar{C}_i \Delta t_i} = [s] \tag{14}$$

$$\sigma^2 = \frac{\int_0^\infty t^2 C dt}{\int_0^\infty C dt} - \bar{t}^2 = \frac{\sum_i t_i^2 \bar{C}_i \Delta t_i}{\sum_i \bar{C}_i \Delta t_i} - \bar{t}^2 = [s^2] \tag{15}$$

$$\sigma_\Theta^2 = \frac{\sigma^2}{\bar{t}^2} \cong 2\frac{\Gamma}{uL} \tag{16}$$

$$E = \frac{C}{m/\dot{q}} = \left[\frac{kg/m^3}{kg/m^3/s}\right] \tag{17}$$

where C is the concentration of the tracer (kg/kg). $\Theta\left(= t/\bar{t}\right)$ is the non-dimensional mean residence time and E is the mean residence time distribution function.

2.4 Solution of model equations

The governing equations (Equations 1-4) were numerically solved by finite volume method using commercial CFD code FLUENT (Ansys Inc., version 15.0)[35]. Governing equations were spatially

15

discretized using the second order upwind scheme. Second order discretization scheme was used for the interpolation of pressure. SIMPLE algorithm was used for pressure-velocity coupling. Transient simulations were carried out using the time step (Δt) as ten thousandth of the space–time, $\tau\left(\Delta t = \tau/10000\right)$. Absolute value of the root mean square residuals for velocities and mass were ensured to be below 10^{-7} and residuals for the energy equation to be below 10^{-10} for each time step to ensure convergence. Maximum of 100 iterations were defined for each time step until convergence was established.

For each case, simulation was initially carried out for time 3τ (where τ is residence time of the fluidic oscillator). It was observed that this time is adequate to establish the flow field and to arrive at a statistically steady solution. After establishing the flow field in this manner, the monitor probes: the static pressure monitored at the monitor point (Figure 1b), pressure drop, logarithmic mean temperature difference, $\left(\Delta T_{LMTD}\right)$ and statistical averaging of the velocity, static temperature and pressure field were activated and statistical averaging was started. Simulations were then further carried out for 5 τ (for averaging purposes). We observed that variation in the velocity contours or PSD obtained at 4 τ and 5 τ is insignificant and therefore averaging of 5 τ was considered to be adequate. Statistical averaging of flow parameters for 5 τ constitutes an averaging of around 20 complete jet oscillation periods. The static pressure data (of time 5τ or more) was used for arriving at the oscillating frequency (f_Z) of the jet using Fast Fourier transformation (FFT) in Matlab[36]. The pressure value at the monitor point was recorded at every time step of the flow simulations. A 20 Hz low pass filter was used to remove higher frequencies. The expected jet oscillation frequencies were less than 10 Hz. 30000 data points were used for FFT from which dominant jet oscillation frequency was identified.

For mixing simulations, mass fraction of the tracer (*m*) and variance σ^2 (details in parameters section) were defined using User Defined Function in Fluent and were monitored at the outlet periodic surface (*O*) of the oscillator at every time-step. The flow in the oscillator using multi species model was simulated up to 6τ or more for arriving a statistically steady state solution for each *Re*. The inner iterations per time step were defined as 150 to ensure that residuals of species fall below 10^{-10} for the coupled flow and species transport equations. The simulated outlet concentration data was used for obtaining RTD curve (*E*) and Dispersion number (*D*) following the equations presented in previous sub-section.

Computational meshes used for numerical solution were generated using blocking technique in ICEMCFD software[35] for the three selected geometries. The mesh or grid blocks were strategically split and placed to ensure high quality refined grid elements near the walls/critical regions, and coarser in the remaining

regions. Key parameters like skew, aspect ratio and Jacobean were used as per the standards (Thompson et al. 1998)[37]. Mesh details along with zoomed view to the mesh at critical regions are shown in Figure 2 for WS geometry and in supplementary information for SL and OD geometry (Supplementary information. Figures S1a and S1b). Grid independency tests were performed using 6 grids of count 0.1 million and 0.2x million (x=1:5) elements for the case of superficial of 0.833 *m/s* (using velocity inlet and pressure outlet boundary condition; $I_1 = I_2 = 0.4167$ *m/s*; *Re* = 769). The mean center line velocity profile was not sensitive to the number of computational cells over the considered range. Therefore, energy dissipation rate per unit mass (ε) of the oscillator (Equation 9), power spectral density (PSD), static pressure at monitored point and jet oscillating frequency $\left(f_z \right)$ were selected for the grid independency study. The influence of number of computational cells on these quantities is shown in supplementary information (Figure S2 and Table S1). The jet frequency, f_z, was found to attain a constant value of 3.21 for grid count above 0.2 million elements. However, to bring the variation of the power spectral density (PSD) below 1%, the number of computational cells require to be around 0.6 million and above. It can be seen from Figure S2 (in supplementary information) that the variation in ε and P_{stat} at the monitored point was found to be below 0.1 % for computational cells above 0.6 million. Therefore, all further simulations were carried out on mesh with number of computational cells as 0.6 million.
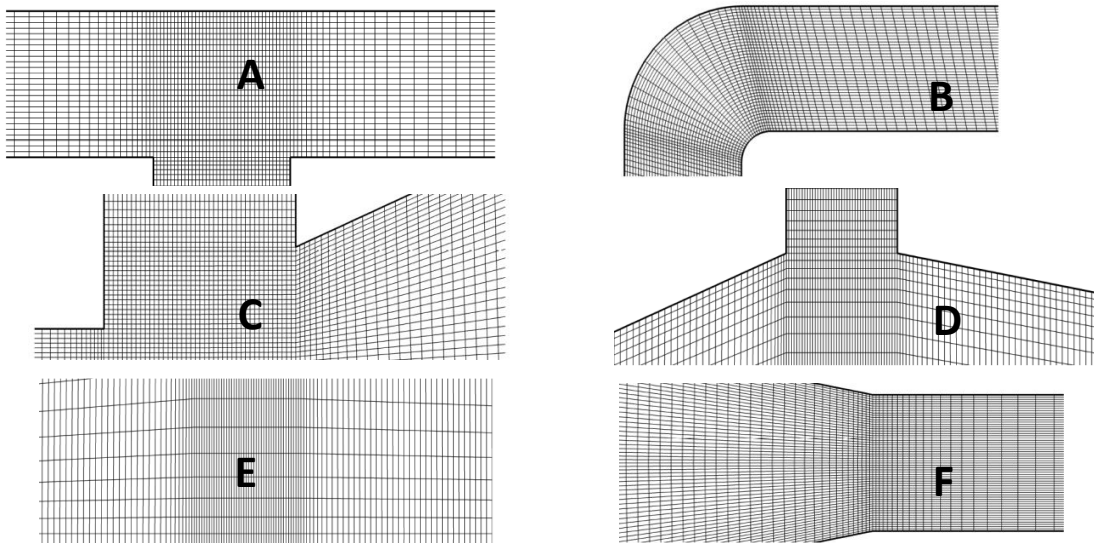

Figure 2: Structured grid images of selected regions of 2D Coanda oscillator WS.
(No. of nodes= 600912; No. of cells=604457; Max. Aspect ratio=12.1; Orthogonal quality=0.92)

Using the 0.6 million mesh, tests for quantifying influence of time step were carried out for a case of velocity of 1.667 m/s ($I_1 = I_2 = 0.833$ *m/s*; *Re* = 1538 for WS). Time step based on space–time formulation

was reduced and increased by one order. No variation in the flow behavior (based on jet oscillation frequency and statistically averaged flow contours) was observed. The maximum oscillation frequency from this study was observed to be below 10 Hz (or time period of 0.1 seconds) for WS. Therefore, the selected time step using space–time formulation (smaller by at least 3 orders compared to the jet oscillation period) is justified.

3. Result and Discussion

In this work, systematic investigations have been carried out to characterize flow, mixing and heat transfer in the three considered oscillator geometries, viz., WS, SL and OD (Figure 1a). Initially, flow simulations were carried out to understand key characteristics of the WS design at different Re and to identify different possible regimes of flow. Based on the insights gained, simulations were carried out for WS, SL and OD designs to understand influence of design and operating conditions on the flow, mixing and heat transfer characteristics. Influence of scale on key characteristics was also investigated for WS and SL designs. The key results are discussed in the following.

3.1 Flow characteristics of oscillators

The free stream jet has an inherently oscillatory nature owing to the flow instabilities above a certain Re (Righolt et al. 2016)[38]. The oscillator design with feedback loops has the capability to set the jet into oscillatory mode either by pressure differential or mass flow through the loops on either sides of the jet. Complex, transient, re-circulatory flow is generated because of these oscillations. A jet flow in a confined chamber and flow regimes based on key dynamic characteristics have been investigated by Lawson and Davidson (2001)[39] and Maurel et al. (1996)[40]. It is important to identify and quantitatively understand different possible flow regimes for the oscillator geometries considered in this work. Various flow regimes are discussed based on the transient simulations carried out with the WS design for Re = 128-1538. In the WS type oscillators, the Coanda effect tries to attach the jet to one of the sides of the mixing chamber wall. If this effect is dominant, the feedback loops become ineffective and flow oscillations will not occur. In order to understand these phenomena, statistically averaged non dimensional mean velocity magnitude contours obtained at different Re are shown in Figure 3. At low Reynolds number like Re = 128, oscillations do not exist. The jet either flows through the central region or attaches to one of the sides of the chamber. The Coanda effect is not strong enough to maintain jet adherence to the chamber wall continuously and for most of the time, the jet passes through the center region (Figure 3a). This regime can be defined as no oscillation regime. With increase in velocity, i.e. for Re = 256, the jet instabilities are encountered. The jet gets adhered to the walls due to strong Coanda effect. This causes the flow to form in an asymmetric flow pattern (Figure 3b). Further increase in Reynolds number (Re = 513 and above), the jet exhibits self-

sustained oscillations. The oscillations are sustained due to the feedback loop effect, (and/or) jet instability and the Coanda effect. This regime is shown by the velocity contours for Reynolds number of 769 (Figure 3c) and 1538 (Figure 3d) where sustained jet oscillations are observed. Another powerful way of examining these oscillations is by looking at power spectral density distributions (PSD) of these oscillations. Simulated power spectral density distributions from a monitored pressure point (Figure 1b for reference) for the corresponding cases are shown in Figure 4.
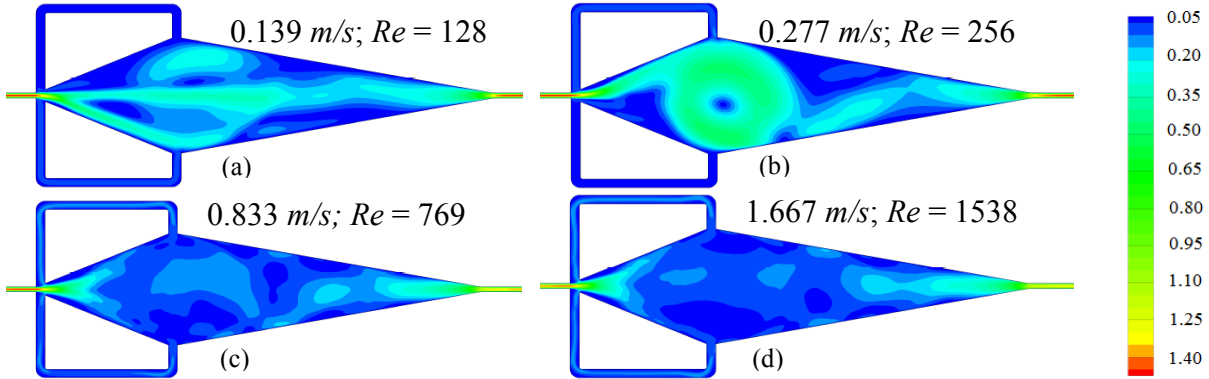

Figure 3: Comparison of time averaged mean velocity contours for WS at different *Re*

It can be seen that at lowest *Re* (128), there are is no oscillation regime and therefore no PSD. At *Re* = 256, the variation in the maximum PSD compared with PSD at other frequencies is observed to be very small, thereby indicating suppression of the jet oscillations. Though a spike in the frequency (f_z= 1.11) is observed, variation of the peak PSD compared to PSD at other frequencies is rather minor (<25%). This small peak is caused due to strong secondary vortices generated in the mixing chamber and not due to jet oscillations. A single dominant frequency is observed at higher *Re* (>513) indicating sustained oscillations and a symmetric jet oscillatory behavior of the oscillator WS. Velocity contours shown in Figure 3c and 3d also show sustained flow through feedback arms confirming the oscillations.

Using the dominant frequency identified from the simulated PSD, average frequencies of jet oscillations and based on which Strouhal numbers were calculated. The observed values of Strouhal number are shown as a function of Reynolds number in Figure 5. It can be seen that the Strouhal number is almost independent of Reynolds number which is in agreement with the published information (Xu and Meng, 2013; Xie and Xu, 2017)[21,23]. The average value of Strouhal number was found to be 0.0026.
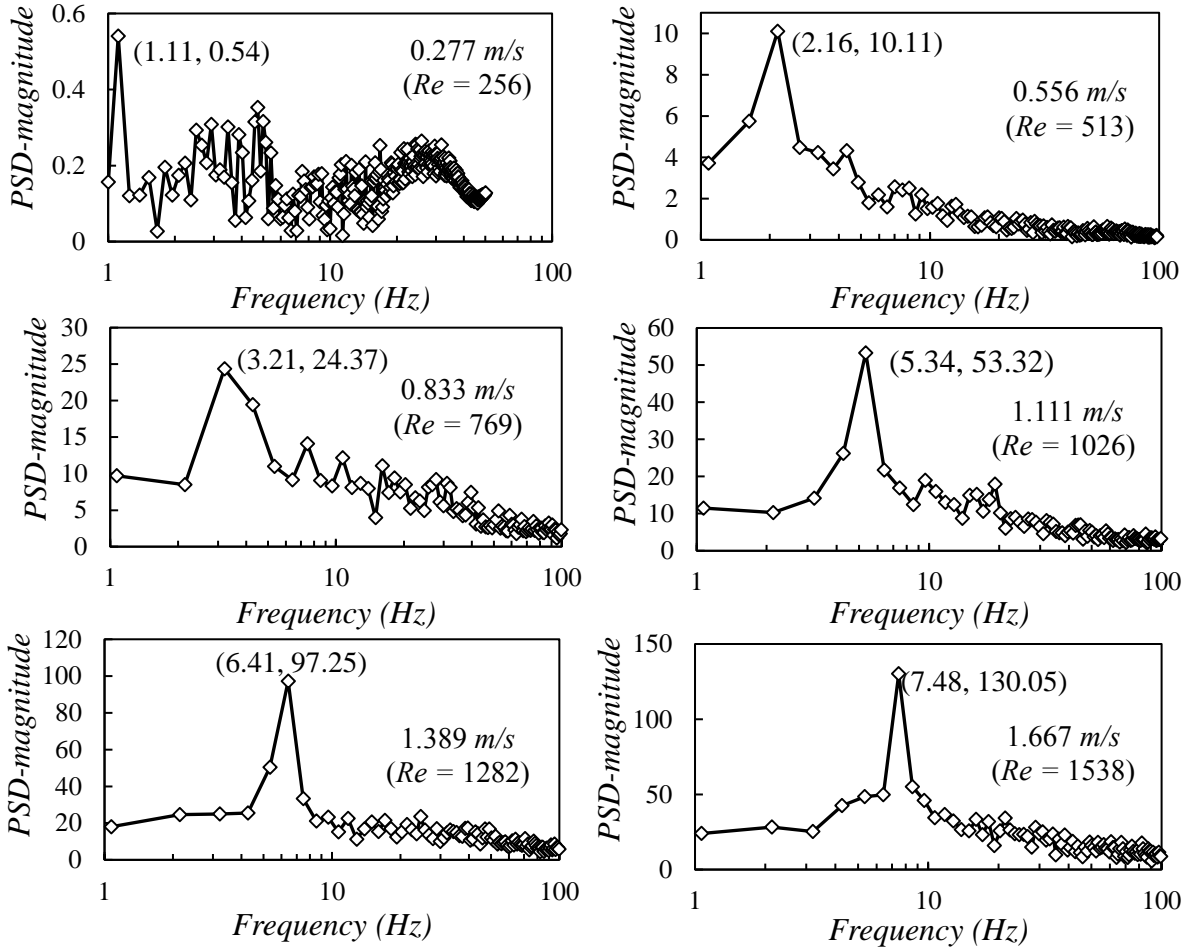
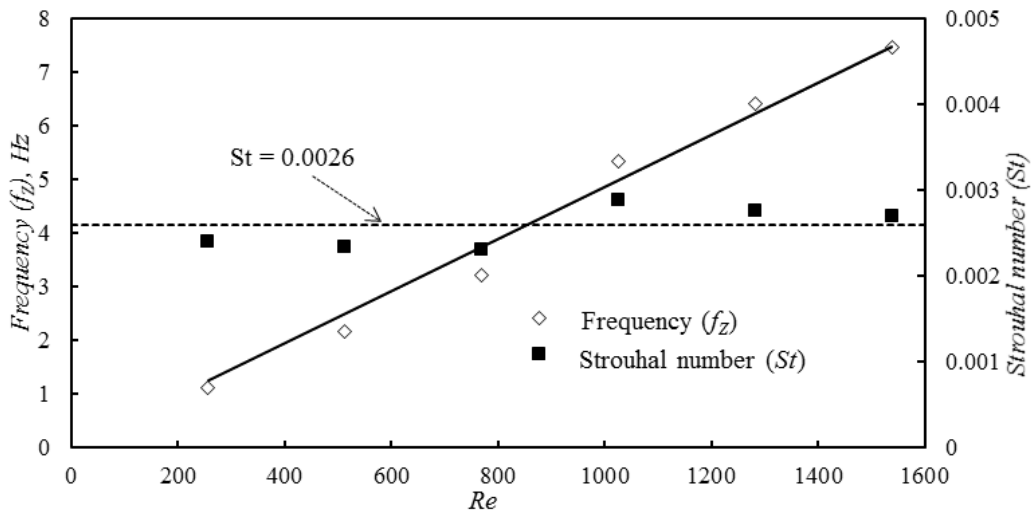Figure 4: Variation in frequency distribution and the peak PSD magnitude with *Re* for the 2D Coanda oscillator WS

Figure 5: Variation in frequency and PSD magnitude with *Re* for the 2D Coanda oscillator WS

20

Spatio-temporal fluctuations in the flow field promote mixing (Roberts and Webster, 2002)[41]. Analysis of such chaotic convection has recently been reported for OD design by Xie and Xu, (2017)[23]. In this work, we define a parameter (ξ) which is dimensionless fluctuating kinetic energy (see Equation 8) to quantify the fluctuations which may be used to relate flow, heat transfer and mixing. Large magnitude of ξ indicates increased interaction and mass transfer between the parcels of the flowing fluid, which ultimately result in enhanced mixing and heat transfer characteristics. Figure 6 shows ξ contours for the three designs of oscillators (WS, SL and OD) at different Re. The ξ results shown in Figure 6 will be useful to interpret simulated results of heat transfer and mixing as discussed in Sections 3.2 and 3.3). The simulated values of flow ratio φ, i.e. ratio of average volume flow rate (obtained from statistical averaged flow time history) through the feedback loop (q_L) to the inlet volume flow rate (q) are shown in Figure 7 for all these considered designs. Based on the analysis of these results, the key flow characteristics of the studied fluidic oscillators are discussed by considering ranges of Re (Re < 128, 128 < Re < 513 and Re > 513) in the following.

Low ≤128 Re regime:

Major purpose of the limbs is to generate sustained oscillating jet due to the asymmetric forces developed in the plane normal to the flow direction instigating recirculation effects (owing to Coanda effect, pressure differential at the limb ends and/or instabilities in the jet). Sustained oscillations have been established in both SL and OD due to these asymmetric forces[11],[23]. The wedge placed in the center of the oscillatory chamber of OD design enables even small movement (away from the axis) in the jet in Y plane to amplify pressure differential at the ends of the symmetric feedback loop (time phase lag in pressure differential between the two loops). Therefore, even at Re (≤128), ξ contour (Figure 6) and volumetric averaged ξ (Figure 7) for OD are observed to have higher magnitude as compared to WS and SL. The OD feedback loops have a diverging inlet compared to converging outlet (Figure 1a). Due to established jet oscillations in the chamber causing an alternating flow on each of the loop inlets, jet oscillations get amplified (concentrated flow on either sides of the wedge). High frequency oscillations in OD design exist even at Re = 90 (93 Hz)[23] allowing alternate switching flow through the limbs (φ = 0.06 in Figure 7). For WS and SL design, the pressure differential generated between the ends of the feedback loops is not strong enough to initiate or sustain any oscillations (due to the diverging chamber section between the inlet and outlet connection, velocity drop and pressure rise transpires). Though flow exists (φ = 0.06-0.08) through the loops at Re = 128, the generated pressure differential is not strong enough to overcome the Coanda effect or set jet instability to amplify any initiated oscillation (by disturbance or by external agency). Therefore, OD design is expected to perform better in terms of heat transfer and mass transfer than WS and SL designs at low Re.

WS design   SL design   OD design

0.138 *m/s*; *Re* =128   0.138 *m/s*; *Re* =128   0.25 *m/s*; *Re* = 91

0.277 *m/s*; *Re* = 256   0.277 *m/s*; *Re* = 256   0.5 *m/s*; *Re* = 182

0.555 *m/s*; *Re* = 513   0.555 *m/s*; *Re* = 513   1 *m/s*; *Re* =364

0.833 *m/s*; *Re* = 769   0.833 *m/s*; *Re* = 769   1.75 *m/s*; *Re* =636

1.667 *m/s*; *Re* = 1539   1.667 *m/s*; *Re* = 1539   2.5 *m/s*; *Re* =909

0   0.005 0.01 0.05   0.1   0.2   0.3   0.4   0.5   0.6   0.7   1   2   4   10
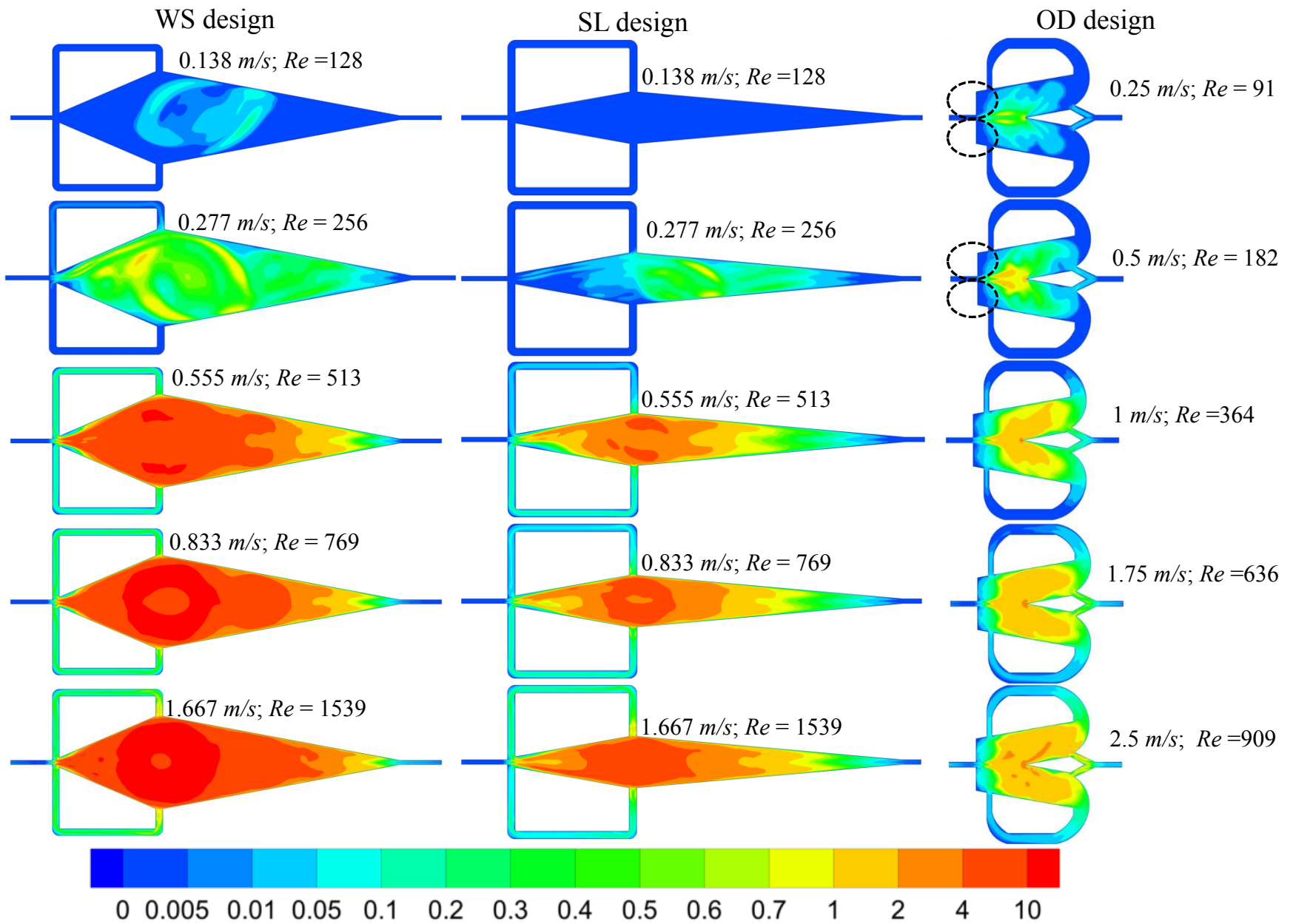
Figure 6: Comparison of non-dimensional fluctuating kinetic energy (ξ) at different *Re* for selected designs
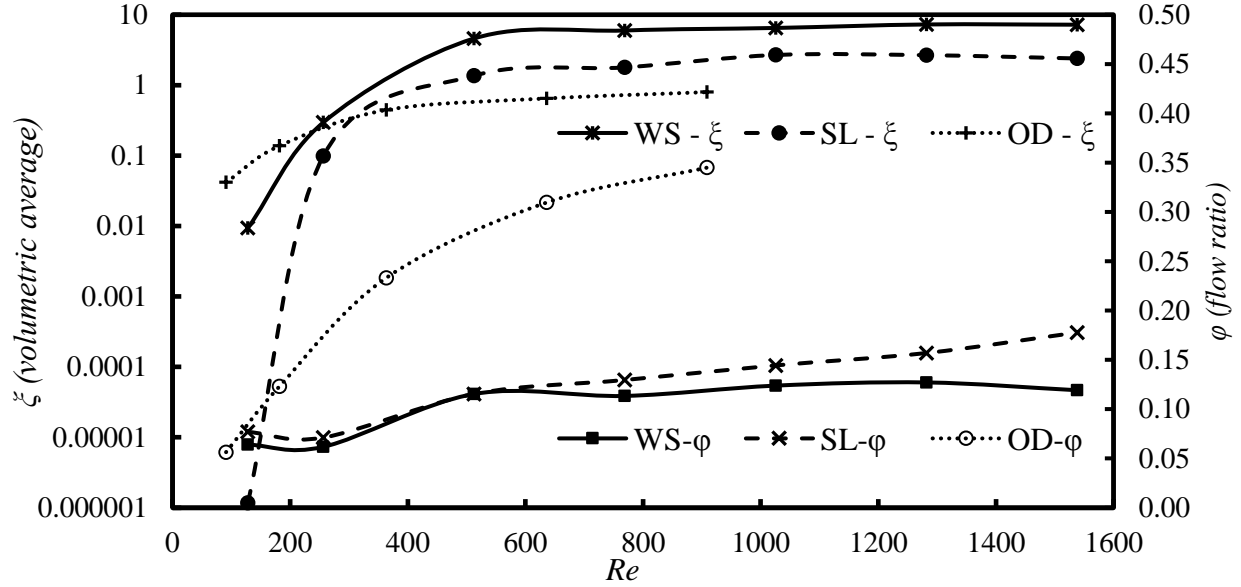
Figure 7: Influence of Reynolds number (Re) on key characteristics of the three selected designs. (a) ratio of averaged feedback loop flow rate to inlet flow rate ($\varphi=q_L/q$) and (b) volumetric averaged non-dimensional fluctuating kinetic energy (ξ).

Medium (182 − 513) Re regime:

In this medium range Re conditions, the pressure differential and its phase lag between the ends of each feedback loops is high enough (due to increased velocity) to overcome the Coanda effect and sustained jet oscillations are established for both WS and SL designs. This results in improvement in the φ and averaged ξ magnitude (Figure 7). The sweeping of the jet generates spatio temporal variation in velocity and can be observed in ξ contours in Figure 6. The sweeping jet generates secondary vortices in the chamber thereby, instigates an active shearing effect in the neighboring fluid (sample vorticity contours for WS shown in Figure S3 in the SI). These vortices continuously undergo, vortex, splitting, merging or generation in the chamber and also within the limbs. During the condition of maximum pressure differential, the fluid flowing into the limbs may undergo separation at the inlet of the limbs and in the bend region. The flow of these vortices within the limbs causes large fluctuations in the velocity and can be seen in the ξ contours shown in Figure 6. Asymmetric flow pattern is established for SL geometry at Re = 256 (due to the Coanda effect dominance), which gets nullified at Re = 513 and above. ξ contours are observed to be almost symmetric for WS design for these *Re* (Figure 6). The dynamic motion of the vortices does not get suppressed for both SL and WS designs and therefore enhancement in mixing and heat transfer can be expected for these cases. For OD design, more flow is observed via feedback limbs (φ is higher than both WS and SL, see Figure 7). Primary reason is due to strategically located inlets of the feedback loops and the wedge. The oscillating jet alternatively gets directed into the limb inlets forcing larger quantity of fluid to pass through it. Also, the wedge ensures maximum pressure differential to be developed between the limb ends. As observed in

23

the flow contours of OD design (also shown in Xie and Xu, 2017)[23] any generated vortices however quickly die out as they flow through the loops mainly due to the smooth curvature and converging shape in flow direction. Therefore, from ξ contour exhibit negligible magnitude within the limbs, though the flow ratio (φ) is quite high (Figure 7) compared to WS and SL designs. Dead zones or KAM tori are distinctly observed in the corner region of chamber inlet and limb outlet at $Re = 181$ as reported by Xie and Xu, 2017[23] in the stream function contours and will be discussed later in Section 3.3.

High (>513) Re regime:

For $Re = 513$ and above, ξ, continues to increase due to augmentation of the vortex dynamics by the oscillating jet. For WS and SL, size and strength of the vortices are not suppressed by the confined walls ensuring rigorous vortex generation, splitting and merging. This is due to the increased flow rate and the jet frequency. WS is having a larger chamber and smaller limbs as compared to SL, and hence, higher values of ξ magnitude (Figure 7) and ξ distribution (both limbs and chamber) are developed in the oscillator. Flow ratio φ, is observed to be higher for SL design as compared to WS and exhibits an increasing trend with Re (Figure 7). For OD, a substantial rise in φ is observed with Re (0.34 for $Re = 909$) but, negligible rise is seen for ξ when compared with WS and SL, indicating the side effects of vortex suppression (in strength and size) by the wedge. Variation of energy dissipation per unit mass for a single periodic unit for the considered designs with Re is shown in Figure 8.
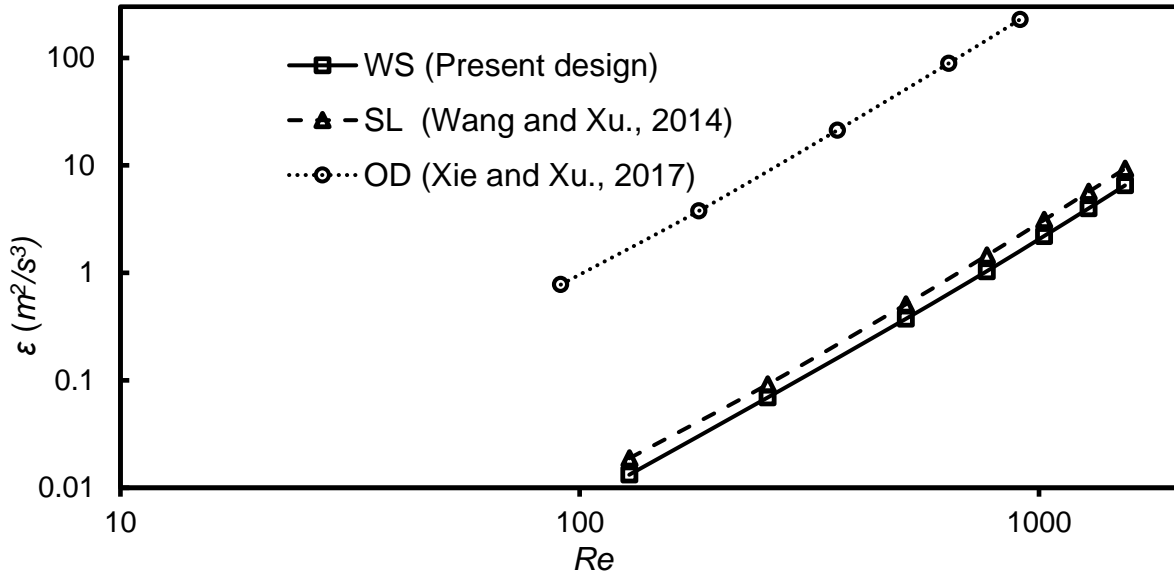

Figure 8: Quantitative comparison of energy dissipation rate per unit mass (ε) for the studied periodic designs with Re.

The energy dissipation rate per unit mass for WS and SL are more or less same while the energy dissipation rate per unit mass for OD is much higher. For industrial applications requiring high productivity, large number of such units would be configured together, WS and SL (preferably WS exhibiting minimum ε) would be more suited from energy requirement perspective as compared to OD. We have compared the energy dissipation rate as obtained from pressure drop and flow rate with that calculated from the product of stress and strain. The variations in both these methods is around 8 %. A detailed comparison is shown in Table S3 of SI by integrating Equation S5. The good agreement between the two ways of calculating energy dissipation rate per unit mass confirms the overall adequacy of numerical simulation parameters (mesh, discretization, time steps and convergence).

3.2 Heat transfer

Fluidic oscillators have exhibited an excellent capability to liquid-liquid extraction process[17]. These oscillators can be expected to perform well for heat transfer applications too, owing to its capability of generating enhanced shearing environment and velocity fluctuations suitable for convective heat transfer. The heat transfer plays a crucial role in establishing the performance of the reactor[42]. Flow dynamics and the jet structure may get modified due to the temperature difference in the confined walls and the jet[43],[44]. Modelling of heat transfer in fluidic oscillators for fundamental understanding of the dynamics has not yet been reported in published literature. Here we present key heat transfer characteristics of the considered three oscillator designs which will facilitate application of these designs for real life applications with heat transfer.

Statistically averaged simulated temperature contours are shown in Figure 9 for WS. At low $Re \leq 256$, large variation in static temperature is observed spatially, indicating the incompetency of the oscillator to transfer heat. A short circuiting behavior is observed similar to what can be seen in the flow features for this range of Re from flow simulations discussed previously. The fluid present in the limbs flowing at substantially lower velocities is exposed to large temperature flux thereby exhibiting temperature almost equal to that of the walls. As discussed previously, Coanda effect dominates over the other unbalanced forces thereby suppressing jet oscillations. At Re above 513, enough differential pressure at the ends of the limbs along with time phase lag between both the limbs is developed to ensure sustained fee oscillations of the jet. The same can be corroborated with the mean fluctuating kinetic energy plot (Figure 7) indicating negligible magnitude for Re below 256 ($\xi \leq 0.29$) as compared to Re above 513 ($\xi \geq 4.6$). For $Re \geq 513$, an improved distribution of averaged static temperature can be observed. Therefore, at higher flow rates, uniformity in the temperature distribution within the reactor can be maintained at high Re. All the fluid parcels entering the mixing chamber are exposed to maximum temperature fluctuations at the entrance for $Re \geq 513$

compared to $Re \leq 256$ where asymmetric temperature fluctuations far from entrance are observed (see statistically averaged temperature fluctuation contours in Figure S4). Chaotic advection plays a primary role in fluidic oscillators for the augmentation in the heat transfer as seen in the contours in Figure 9 and Figure S4 for WS. The variation of simulated Nusselt number (*Nu*) with *Re* for the three selected designs is shown in Figure 10 along with straight circular pipe flow obtained from the literature[45]. The variation of the heat transfer enhancement ratio (η) indicating the combined effect of flow and heat transfer together when compared to straight circular pipe flow is shown in Figure 11 for the selected designs[46].
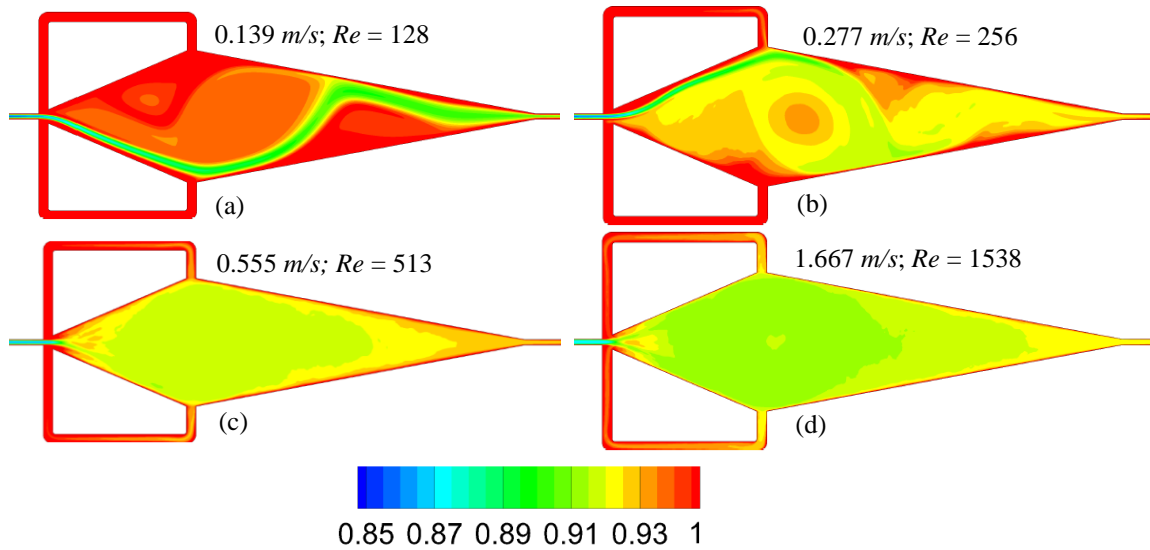

Figure 9: Variation of statistically averaged temperature contours on the periodic unit of WS design.
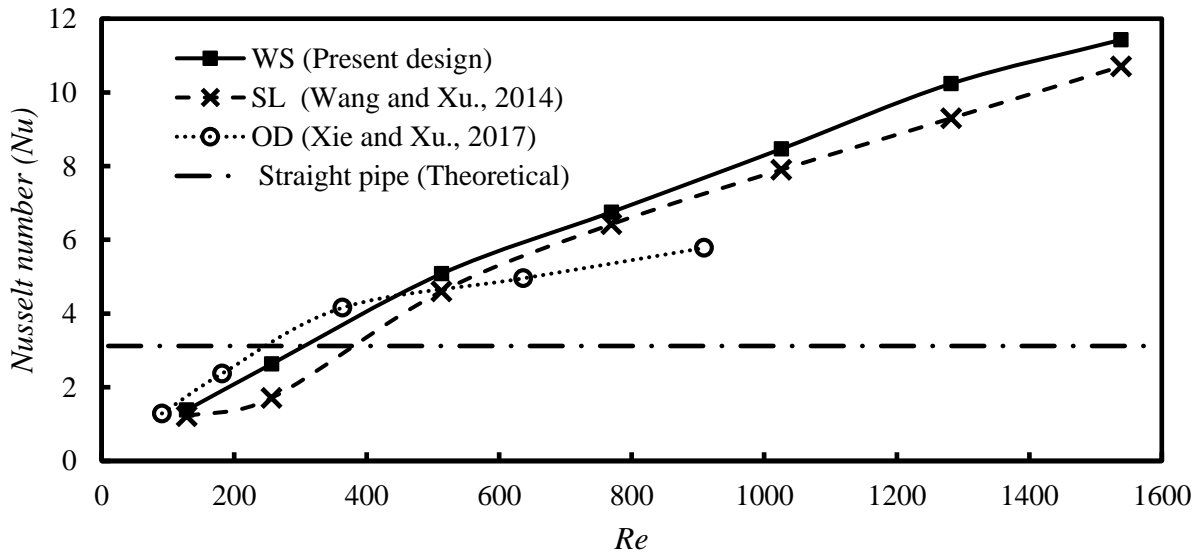(non-dimensional with wall temperature)

Figure 10: Variation of Nusselt number with *Re* for different geometries
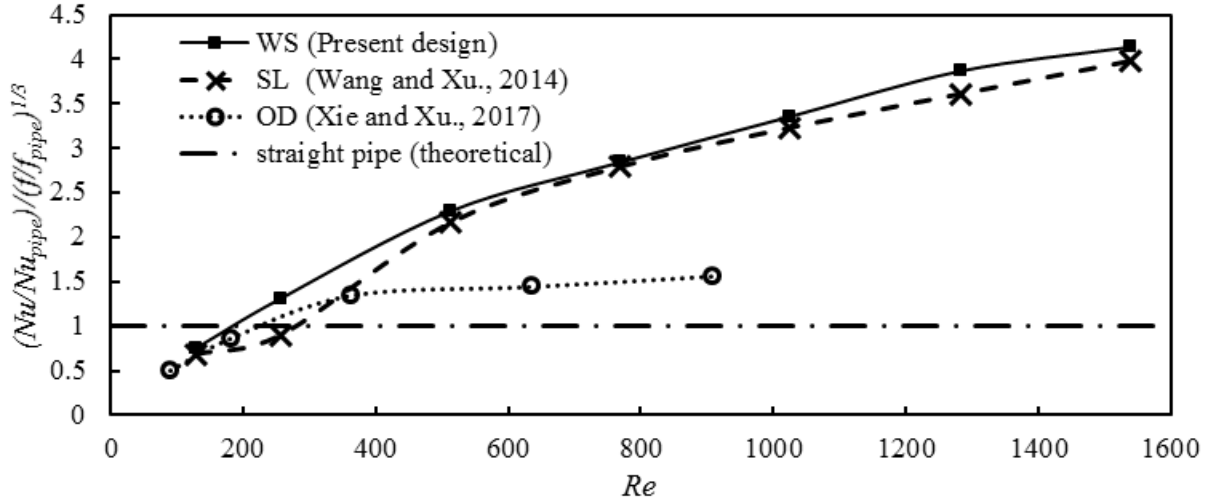(Theoretical values of straight pipe from Shah and London, 1978)[46]

Figure 11: Variation of heat transfer enhancement ratio with *Re* for different designs.
(Theoretical values of straight pipe from Shah and London, 1978)[46]

With increase in *Re*, as expected *Nu* increase for all the three selected designs. Nusselt number for WS and SL design were found to be almost same for *Re* = 128 (Figure 10). Coanda effect is dominant or no significant unbalanced forces exist at this low *Re*. At *Re* = 256, *Nu* for WS is 1.53 times more than SL (Figure 10). The reason for higher *Nu* can be attributed to the realized jet oscillations (though suppressed) by the WS geometry as compared to no oscillations for SL (discussed in flow Section 3.1 in detail). Therefore, SL at the same *Re* exhibits lower η value (Figure 11) indicating maximum flow exiting the domain undisturbed, or with insignificant variation in thermal response (due to Coanda effect). With further increase in *Re* say 513 and above, a rise in *Nu* (Figure 10) and η (Figure 11) is observed for both WS and SL. Magnitude of *Nu* for all simulated *Re* is higher for WS as compared to OD, owing to the increased chamber dimension and reduced limb length. The flow regimes (based on Figure 4 and 6) and the volumetric average of non-dimensional fluctuating kinetic energy ξ (Figure 7) also support these trends. When compared with straight pipe,[46] *Nu* is higher for both WS and SL above *Re* = 400 (assuming linear trend in *Nu* V/S *Re*). η enhancement is more than 1.5 times when compared to straight pipe (Figure 11) . The OD design has higher value of *Nu* at *Re* = 91 as jet has achieved self-sustained oscillations. *Nu* keeps on increasing with increase in *Re* for OD up to *Re*=364 (Figure 10). This increment was mainly due to the acceleration of the fluid through the strategically located limbs causing higher heat transfer even at low *Re*. With further increase in *Re* i.e. above 636, the slope of increment decreases. Reason can be attributed to lower realized ξ magnitude and ξ spatial distribution. When compared with straight pipe, *Nu* and η is higher for OD above *Re* = 375. It can be seen from Figure 11 that the WS configuration exhibits better performance than any other selected design, followed by SL. Both WS and SL show a linearly increasing trend with *Re*

with maximum of about 4 for *Re* greater than 1500. The η values for OD design are much lower and do not increase beyond 1.6.

WS and SL design for *Re* lying in the self-sustaining oscillation regime (*Re*≥256 for WS and *Re* ≥ 513 for SL), improved performance in both *Nu* and *η* is observed. WS and SL perform better than OD for Re ≥ 400. At low *Re* (≤400), OD exhibits an improved heat transfer performance compared to WS and SL design. WS is a better design for exhibiting higher *Nu* and *η* at all *Re*. The least operating *Re* based on heat transfer enhancement efficiency is 300, which will ensure performance of the design better than the straight pipe.

3.3 Mixing and residence time distribution

Characterization of continuous flow reactor systems are based on combination of hydrodynamics, mixing intensity (I_M) and residence time distribution (RTD) realized by the flow in the design[47]. Both numerical and analytical methods have been developed and successfully utilized in characterization of reactors for multiphase/multispecies flow[48–50]. Analytical approach in a reactor constituting an oscillatory jet is quite complex due to the dynamic chaotic advection, thereby urging experimental or computational investigations[51]. In this work, a computational approach, verified using the standard practices, is used for simulating multispecies flow in the selected oscillator designs[45,52]. Firstly, mixing studies were carried using water and tracer as fluid medium for the three selected designs at different *Re*. An attempt is made to relate the defined regimes of flow, and non-dimensional fluctuating kinetic energy (ξ) with the mixing characteristics of the respective designs. Residence time distribution (RTD) and effective dispersion numbers for the selected oscillator designs were then quantified as a function of Reynolds number.

Figure 12 shows an instantaneous mass fraction (MF) contours at difference selected *Re*. All the contours have been generated at non-dimensional time of $\theta = 6$. MF magnitude corresponding to 0 or 1 indicates presence of water or tracer in the corresponding location, whereas MF magnitude of 0.5 indicates 50 % of each of these fluids well mixed with one another. For all the considered designs, the unmixed jet is exposed to chaotic advection as it flows into the oscillating chamber. The jet is broken down by the active vortices present within the chamber, jet oscillation and the alternative mass flow through the limbs. Variation of I_M with non-dimensional time (θ) for the three designs has been shown in Figure 13 for same mass flow rate through them. Mixing intensity increases with time and is observed to attain a stable condition above non dimensional time of $\theta = 3$ (with few exceptions which are discussed later). A quantitative comparison of the time averaged mixing intensity with *Re* is shown in Figure 14 for all the three selected designs at different *Re*.
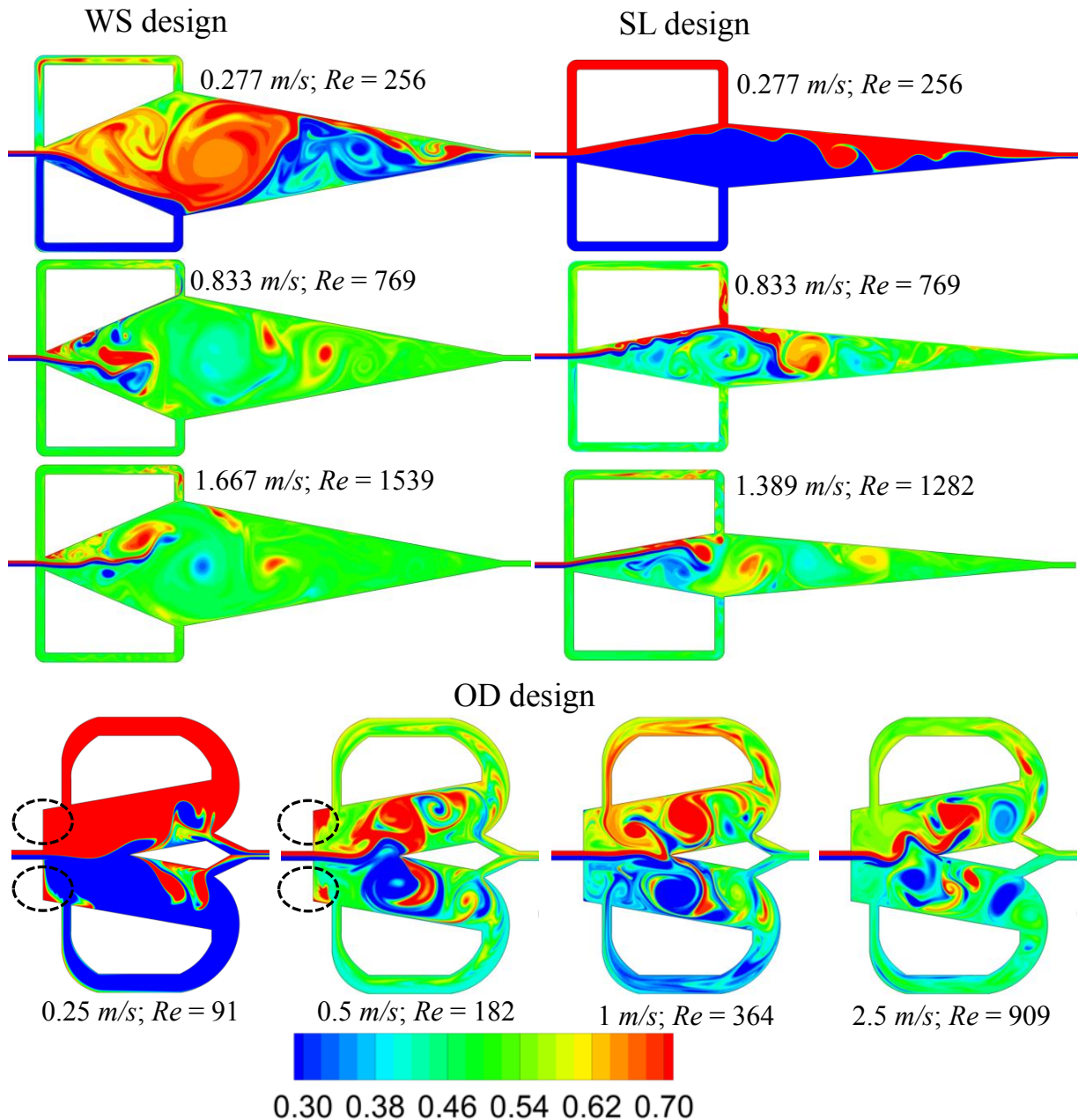
Figure 12: Instantaneous mass fraction contours (MF) for the three selected designs at selected *Re*.

For WS design, at *Re* ≤ 256 (Coanda dominant regime), there are inadequate jet oscillations (Figure 4) and therefore inadequate mixing (Figure 12). For SL design at *Re* = 256, this effect is even more pronounced as it lies in the 'no oscillation regime' (Figure 12). The reduced chamber dimensions of SL as compared to WS also reduces the pressure differential generated between the ends of each limb. This ultimately suppresses the vortex dynamics and no substantial mixing is observed. At Re ≥ 513, improved mixing was observed for both WS and SL throughout the mixing chamber and in both of their respective limbs. The outlet mass fraction is in the range of 0.45 – 0.55 indicating good mixing (Figure 12).
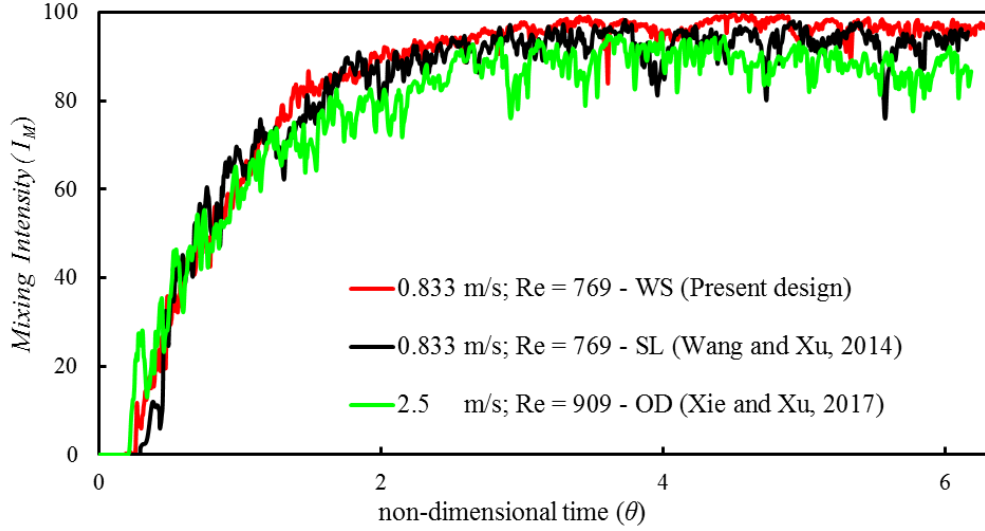
Figure 13: Variation of mining intensity for single unit of different studied geometries considered for same volume flow rate (60 ml/min assuming 2 mm width for the selected geometries)
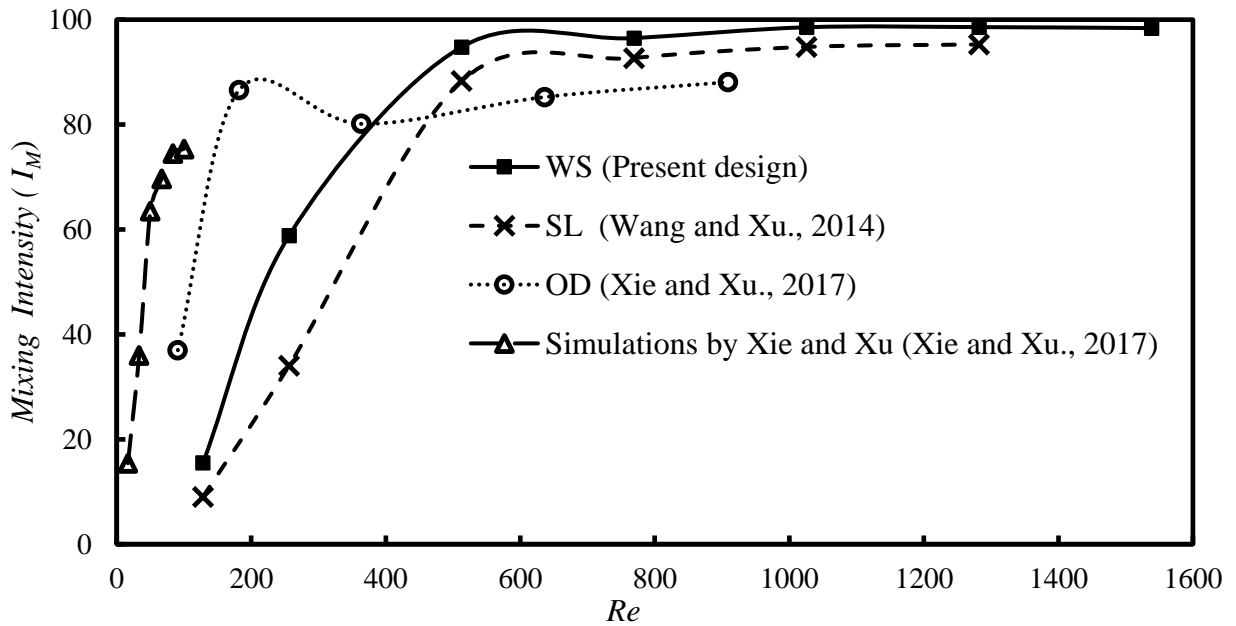
Figure 14: Variation of mixing intensity (I_M) with Re for different selected designs
(I_M is represented in %)

Spatial distribution of tracer mass fraction in WS and SL designs (Figure 12) can be directly corroborated to spatial distribution of ξ magnitude contours shown in Figure 7. The volumetric averaged ξ for WS and SL in Figure 7 indicates negligible magnitude (below 0.29) for flow lying in the 'No oscillation regime' and 'Coanda dominated regime'. Same can be seen in the Figure 14, indicating a smaller value of statistically stable mixing intensity (I_M) for these two regimes. At higher Re ($\geq$ 513), mixing intensity is

above 80% for both WS and SL (Figure 14), and follows an increasing trend with *Re*. Improvement in mixing above this *Re* can also be interpreted from the ξ plot indicating a strong relationship between mixing and ξ (Figure 7). WS design exhibits higher volumetric averaged ξ as compared to SL for all the considered *Re* which results in better mixing in WS design as indicated by I_M variation with *Re* (Figure 14). For WS and SL designs, I_M variation does not achieve a stable value at *Re* = 256 (Figures S5 and S6 in SI). The mixing intensity is otherwise found to attain a steady value after $\theta = 3$ for all the other simulated *Re* (Figures S5 - S7 in SI). Periodic oscillation in mixing is observed at this *Re* indicating the dominant Coanda effect suppressing the oscillation, thereby the mixing.

As discussed in Section 3.1, WS and SL designs mainly work on the principle of allowing the generated vortices to create chaotic motion within the mixing chamber with the aid of Coanda effect, pressure differential and jet instabilities. OD design does not have any wall near to the jet, thereby rely on flow deflection into the auxiliary compartments created by the wedge. The working primarily depends on mass flow through limbs and jet instabilities, whereas weakly dependent on Coanda effect between the jet and wedge. Mixing enhancement is realized due to the strong circulation within the limbs and the oscillating chamber. Due to high frequency jet oscillations, the contact area between the adjacent layers of jet stream increases which further aids in mixing. This leads to engulfment between the jet layers, further leading to chaotic flow.[53] Even at low *Re*, jet is set into oscillatory mode which ensures the jet streams to get diffused along the flow path and on both sides of the wedge. Primary driving force for mixing for OD design, i.e., the mass flow through the limbs is non-substantial ($\varphi = 0.06$) for *Re* = 91. Therefore, a lower value of (I_M) is realized at the outlet as shown in Figure 14. With increase in *Re*, significant increment in the mass flow through the limb is realized, thereby increasing the I_M (Figure 14). Same can be inferred from the Figure 12 indicating improvement in tracer distribution with *Re*. The tracer distribution through the limbs (Figure 12 show the tracer mass fraction is close to either 0 or 1) indicate that the limbs are non- active participants at *Re* = 91. As *Re* increases, the tracer distribution improves both in the limbs and the oscillating chamber. Unmixed fluid present in the vortices has an opportunity to skip through the narrow outlets between the chamber walls and the wedge without entering into the limbs. WS and SL designs have a design advantage of long converging aft part of the oscillating chamber and large chamber size. Larger chamber size ensures efficient utilization of the formed vortex strength and provides them freedom for generating rigorous chaotic motion. The long converging aft part of oscillating chamber ensures enhanced energy dissipation and therefore enhanced mixing. The realized I_M for OD design is below 88% at *Re* = 909 (beyond which energy dissipation is too high) while SL and WS have $I_M \geq 90\%$ for *Re* of and above 803.

The OD design exhibits a KAM tori region for $Re \leq 182$ ($u \leq 0.5$ m/s) which can be visualized in the form of stagnated mass fraction of water (MF = 1) within it (shown using black dotted line in Figure 12). A simulation was performed at $Re = 182$ (0.5 m/s) where statistically steady solution obtained for OD design with water as single primary phase. Later, tracer was injected into the domain to locate the KAM tori region. As seen in Figure S8, the KAM tori region could easily be visualized and quantified (indicated by red line at $\theta = 3$, 4 and 5) using this methodology. Non-significant variation in its shape is observed indicating it to be a major region for the non-uniformities in the particle retention within the domain. This region vanishes for Re $\geq$364 ($u \geq 0.5$ m/s) and can be confirmed from tracer mass fraction (in the range of 0.3 to 0.7 from Figure 12). This observation is in agreement with the simulations and analysis performed by Xie and Xu (2017)[23] using Poincaré mapping. Computational studies for mixing intensity calculations for OD design were done by Xie and Xu, 2017[23]. The trend of variation in I_M is observed to be the same, but there is substantial variation in the obtained I_M magnitude (Figure 14). This may be due to the variation in the geometric design as the exact dimension of curvature of the limbs and the mixing chamber is not reported. It is also important to note that number of computational cells used by Xie and Xu (2017)[23] for their simulations were 0.074 million compared to 0.5 million cells used in our simulations for OD design. It is interesting to note that the WS and SL designs do not exhibit any dead zones.

In order to quantify extent of back mixing in the considered oscillator designs, residence time distributions were simulated using the methodology discussed in Section 3.2. Above 99.5% of the tracer collected at the outlet has been considered as minimum criteria for these RTD simulations. Using the profiles of average tracer mass fraction at the outlet and following standard procedure, the E-θ curves were generated. For WS and SL, accumulation of tracer was observed for $Re = 128$. Therefore, generation of E-θ curve for this Re is not possible and can be defined as minimum benchmark criteria for carrying out chemical reactions for these selected designs. A sample snapshots of tracer mass fraction are shown at different instances for WS design in Figure 15 for $Re = 1328$. As seen in this figure, the tracer concentration in the domain keeps on decreasing as it spreads within the domain mainly by chaotic advection as discussed previously. A sample of RTD curves at two Reynolds numbers is shown in Figure 16a for WS geometry (and in Figures S9 - S11 along with the mass tracer time history collected at the outlet). RTD curves from an ideal CSTR and plug flow reactors are also shown in this figure as a reference. The simulated $E - \theta$ curve indicate the presence of chaotic and oscillatory flow which is quite different than a response seen for the non-oscillating passive mixers[45,54]. Dispersion numbers estimated from the simulated RTD curves as a function of Re are shown in Figure 16b. It can be seen that at high Re, all the three oscillators exhibit more or less constant dispersion numbers. The dispersion number of SL and WS is almost half of as the dispersion number of OD.

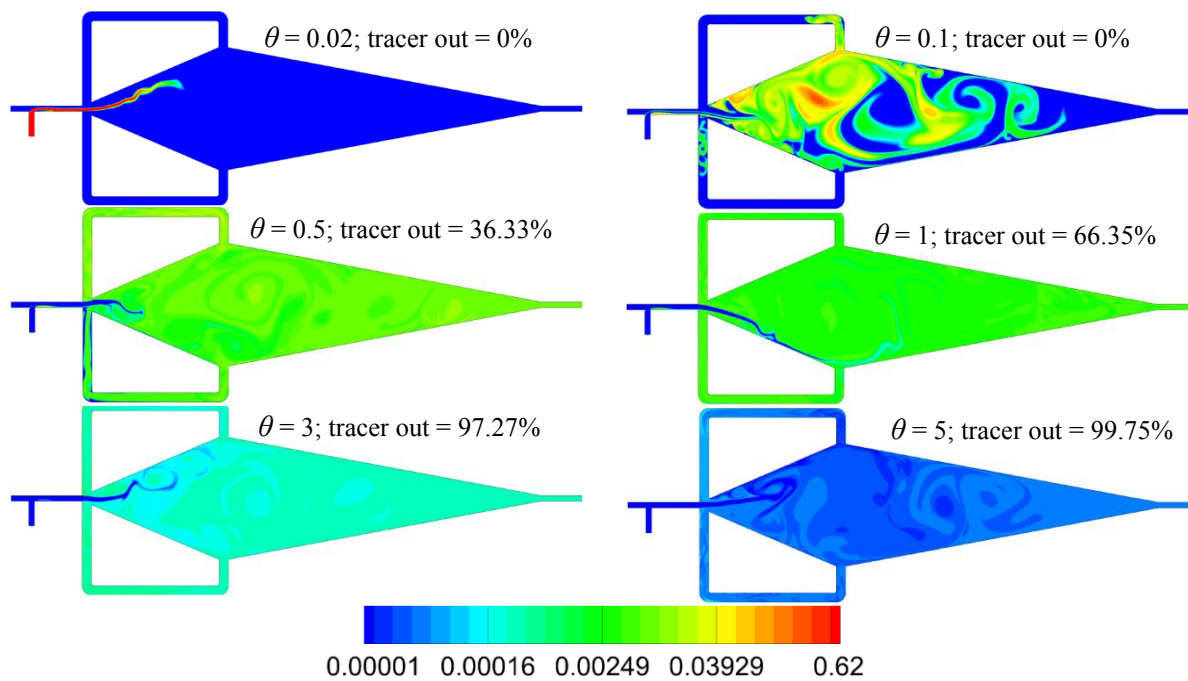Figure 15: Sample tracer contours (at 1.667 *m/s*; *Re* = 1538) at different time instants indicating the

percentage of tracer left from the 2D Coanda oscillator WS ($\theta = \dfrac{t}{\tau}$, where θ is non-dimensional time).
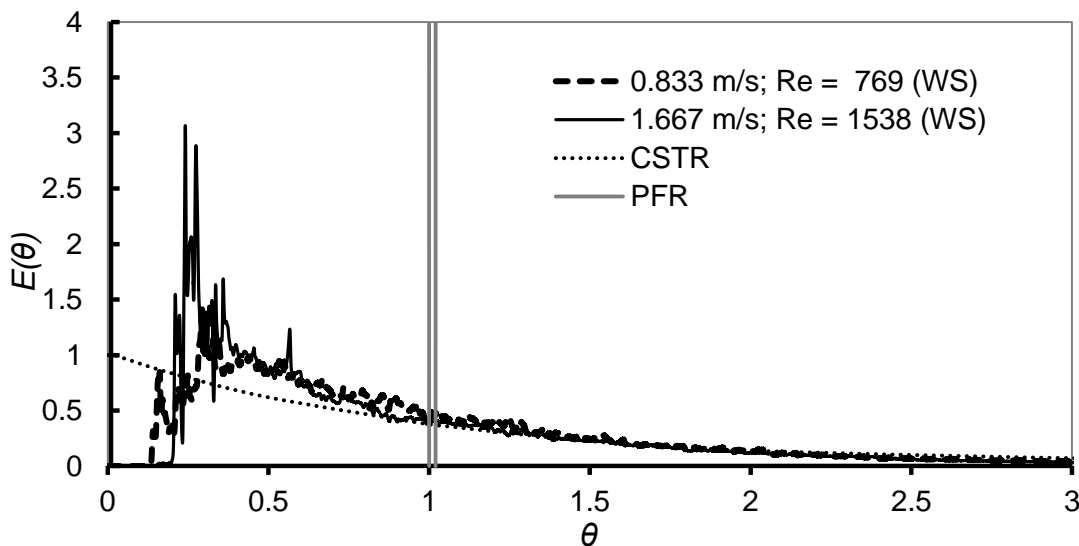

Figure 16a: Comparison of RTD response for different types of mixers/reactors.
(RTD Response for PFR has been shown on secondary axis to accommodate all the reactors in same plot)
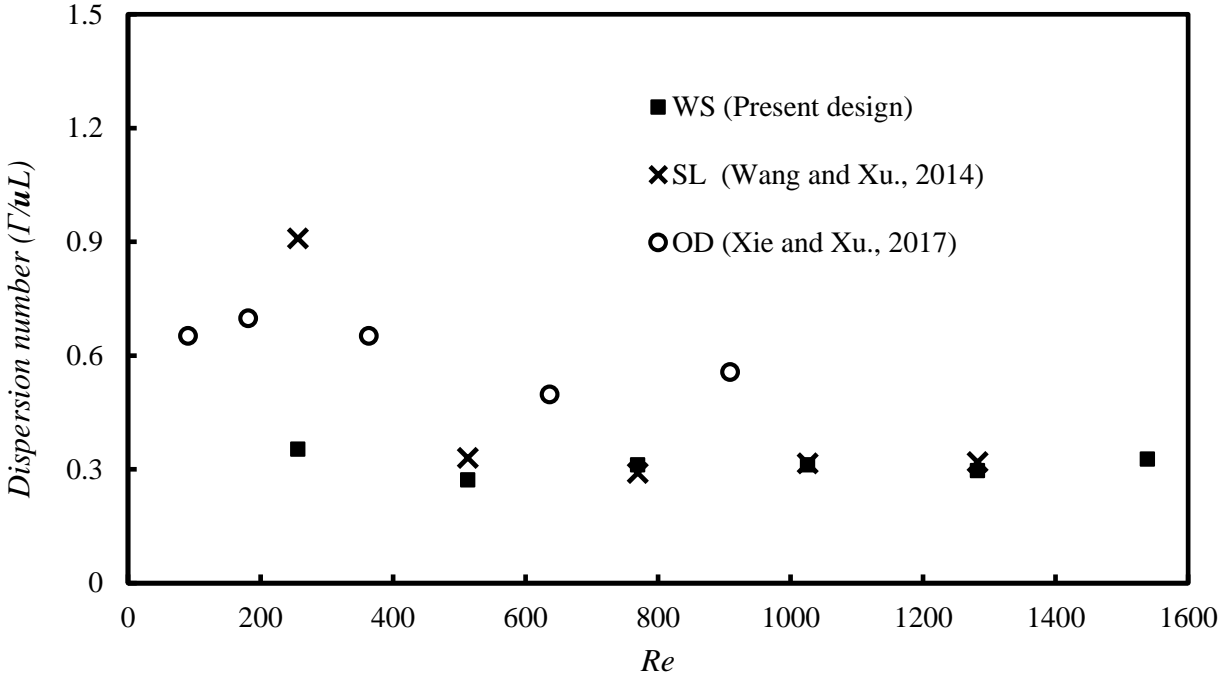
Figure 16b: Variation of Dispersion number with *Re* calculated using Dispersion model[34] for the selected designs

The dispersion number ($\frac{\Gamma}{uL} \cong \frac{\sigma^2}{2\bar{t}^2}$) depends on variance of residence time distribution and mean residence time. The mean residence time, $\bar{t}$, for the WS design is higher compared to OD because of the larger chamber volume. The OD design also exhibits wider residence time distribution because of the relatively low velocity regions existing in the oscillator due to its shape (see Figures S9 and S11 in supplementary information). The combined effect of lower $\bar{t}$ and high σ^2 for OD at any *Re* results in lower dispersion number for WS compared to the OD configuration. The knowledge of dispersion number will be useful when interpreting experimental data obtained using these fluidic oscillators. The quantitative information about the mixing and dispersion of these oscillators will also be useful when series of oscillator units are necessary for realizing adequate residence time to achieve desired reactions or any other applications.

The results presented here will be useful to design prototypes and experiments for characterizing these fluidic oscillators. The results also provide key insights on relationship between design and operating parameters and flow – heat transfer – mixing characteristics of the fluidic oscillators. Further experimental characterization and additional numerical simulations with 3D configurations based on the results presented here will hopefully pave the way for better designs as well as systematic guidelines for optimization of fluidic oscillators for variety of process intensification applications.

4. Conclusions

In this work we computationally investigated flow, heat transfer and mixing for three designs of fluidic oscillators. Two of these designs were taken from the published studies and one of the designs was proposed in this work. Unsteady flow in these fluidic oscillators was characterized using variety of ways including a new non-dimensional parameter, ξ, representing fluctuating kinetic energy. Different flow regimes were identified. Three flow regimes were observed: no oscillation regime, intermediate regime where oscillations are suppressed due to jet adhesion to wall and vigorous oscillations regime. The parameter, ξ was found to be useful indicator for estimating mixing, RTD and heat transfer. Results on heat transfer and residence time distributions in these fluidic oscillators are reported for the first time. Higher mass flow through the limbs or higher oscillating frequency of the jet were not found to be deciding factors for achieving enhanced mixing, RTD and heat transfer within the oscillators. Out of the three oscillator designs investigated here, dead zones were not present in WS and SL designs unlike in the OD design. Chaotic advective flow was more pronounced in WS and SL designs compared to the OD design for Re above 513. WS exhibits minimum energy dissipation per unit mass for all the studied Re followed by SL. The dispersion number of SL and WS is almost half of as the dispersion number of OD. The modified design WS was observed to perform better than SL in all the considered aspects at all Re. Performance of SL and WS from mixing, RTD, heat and mass transfer characteristics was better than OD for all the studied parameters ($Re \geq 513$) (based on energy dissipation rate per unit mass, non-dimensional kinetic energy fluctuations, heat transfer enhancement ratio, mixing intensity and dispersion number). The approach and results presented in this work have provided useful insights which will be useful for selection and optimization of fluidic oscillators for different applications. We are currently extending this work for multiphase flow application in fluidic oscillators which will be published separately. We hope that the work will stimulate further research on tailoring fluid dynamics of these oscillators for expanding their application horizons.

Notations

A	Total area of specified region or elemental cell
A_W	Total area of heated walls
A_{jet}	Area of the jet
V_R	Volume of the oscillator
q	Volume flow rate of the fluid through the oscillator inlet
q_L	Average volume flow rate of the fluid through the limbs
P_i	Perimeter of the selected surface
$I_1, I_2, O, w_1, C_L, H_L, t_L, W_T$	Lines/Surfaces defining geometry/boundary conditions of the domain
L	Length of the unit oscillator in flow direction

w	Depth of the oscillator
D_H	Hydraulic diameter
T	Temperature
T_W	Wall temperature
T_{in}, T_{out}	Fluid temperature at the inlet and outlet
T_{LMTD}	Logarithmic mean temperature difference
$\dot{Q}$	Heat input to fluid through wall
C_P	Specific heat of the fluid at constant pressure
h_{avg}	Average convective heat transfer coefficient
k	Thermal conductivity
m	Mass of the fluid under consideration
$\dot{m}$	Mass flow rate
m_k	Mass ratio of species k
D_{km}	Mass diffusivity of the mixture of species k (in suffix)
C	Concentration of the tracer
E	Mean residence time function
I_M	Intensity of mixing
f	Frictional factor
f_Z	Frequency
t	Time
$\bar{t}$	Mean residence time
$\boldsymbol{u}$	Velocity vector
$v_x, v_y, \acute{v}_x, \acute{v}_x, \bar{v}_x, \bar{v}_y$	Total, fluctuating and mean velocity components
P	Static pressure
Re	Reynolds number
St	Strouhal number
Nu	Nusselt number
η	Heat transfer enhancement ratio
D	Dispersion number

Greek Letters

ρ	Density, kg/m^3
μ	Dynamic viscosity, $kg/(m\,s)$
ϑ	Kinematic viscosity, m^2/s
τ	Space-time of the fluid in the oscillator, s
ε	Energy dissipation rate per unit mass, m^2/s^3

$\bar{\bar{\tau}}$	Stress tensor (N/m^2)
θ	Non dimensional time
ξ	Non dimensional fluctuating kinetic energy
φ	Flow ratio (limbs/inlet)
σ	Variance

Abbreviation

CFD computational fluid dynamics

RTD residence time distribution

PSD power spectral density

MF mass fraction

REFERENCES

[1]   V. Hessel, H. Löwe, F. Schönfeld, *Chem. Eng. Sci.* **2005**, *60*, 2479.

[2]   C. J. Campagnuolo, H. C. Lee, Review of some fluid oscillators, Washington DC **1969**.

[3]   C. J. Campagnuolo, S. E. Gehman, Flueric pressure and temperature insensitive oscillator for timer application, Washington DC **1968**.

[4]   L. Pichini, Pneumatic oscillator using a vortex amplifier, Massachusetts Institute of Technology, **1967**.

[5]   C. Spyropoulos, *Proc. fluid Amplif. Symp.* **1964**, *III*, 27.

[6]   J. R. Tippetts, *J. Mech. Eng. Sci.* **1973**, *15*, 392.

[7]   P. H. Wright, *J. Phys. E.* **1980**, *13*, 433.

[8]   T. Shakouchi, *J. Dyn. Syst. Meas. Control* **1989**, *111*, 535.

[9]   V. Tesař, C.-H. Hung, W. B. Zimmerman, *Sensors Actuators A Phys.* **2006**, *125*, 159.

[10]   J.-T. Yang, C.-K. Chen, K.-J. Tsai, W.-Z. Lin, H.-J. Sheen, *Sensors Actuators A Phys.* **2007**, *135*, 476.

[11]   J. Wang, C. Xu, *Chem. Eng. Technol.* **2014**, *37*, 535.

[12]   C. Xu, Y. Chu, *Chem. Eng. J.* **2014**, *253*, 438.

[13]   F. Rehman, G. J. D. Medley, H. Bandulasena, W. B. J. Zimmerman, *Environ. Res.* **2015**, *137*, 32.

[14]   H. J. Schmidt, R. Woszidlo, C. N. Nayeri, C. O. Paschereit, *Exp. Fluids* **2017**, *58*, 106.

[15]   T. Beatus, R. H. Bar-Ziv, T. Tlusty, *Phys. Rep.* **2012**, *516*, 103.

[16]   C. Xu, Y. Dai, *Ind. Eng. Chem. Res.* **2015**, *54*, 6551.

[17]   C. Xu, T. Xie, *Ind. Eng. Chem. Res.* **2017**, *56*, 7593.

[18]   J. Gregory, M. N. Tomac, "A Review of Fluidic Oscillator Development," 43rd Fluid Dynamics

Conference, AIAA, Reston, Virginia, 24 June **2013**.

[19]   O. Krüger, B. C. Bobusch, R. Woszidlo, C. O. Paschereit, "Numerical Modeling and Validation of the Flow in a Fluidic Oscillator," 21st AIAA Computational Fluid Dynamics Conference, AIAA, Reston, Virginia, 24 June **2013**.

[20]   J. R. McDonough, R. Law, J. Kraemer, A. P. Harvey, *Chem. Eng. Res. Des.* **2017**, *117*, 228.

[21]   C. Xu, X. Meng, *Sensors Actuators A Phys.* **2013**, *189*, 55.

[22]   D. Pal, *The Coanda-effect oil-water separator : a feasibility study*, Civil Engineering Laboratory, Naval Construction Battalion Center, Port Hueneme, California, **1974**.

[23]   T. Xie, C. Xu, *Chem. Eng. Sci.* **2017**, *171*, 303.

[24]   V. Tesař, *Chem. Eng. Res. Des.* **2009**, *87*, 817.

[25]   V. Tesař, *J. Vis.* **2001**, *4*, 51.

[26]   V. Tesař, S. Zhong, F. Rasheed, *AIAA J.* **2013**, *51*, 397.

[27]   B. C. Bobusch, R. Woszidlo, O. Krüger, C. O. Paschereit, "Numerical Investigations on Geometric Parameters Affecting the Oscillation Properties of a Fluidic Oscillator," 21st AIAA Computational Fluid Dynamics Conference, AIAA, San Diego, CA, **2013**.

[28]   R. Woszidlo, F. Ostermann, C. N. Nayeri, C. O. Paschereit, *Exp. Fluids* **2015**, *56*, 125.

[29]   C. Xu, S. Jing, Y. Chu, *AIChE J.* **2016**, *62*, 3685.

[30]   V. Tesař, *Sensors Actuators A Phys.* **2015**, *234*, 158.

[31]   B. C. Bobusch, P. Berndt, C. O. Paschereit, R. Klein, "Active flow and combustion control," *Notes on Numerical Fluid Mechanics and Multidisciplinary Design*, **2015**, Vol. 127, p. 281.

[32]   V. V Ranade, *Computational Flow Modelling for Chemical Reactor Engineering*, 1st edition, Academic Press, **2002**.

[33]   P. Nag, *Engineering Thermodynamics*, 5th edition, Tata McGraw-Hill Publishing Company Limited, **2013**.

[34]   O. Levenspiel, *Ind. Eng. Chem. Res.* **1999**, *38*, 4140.

[35]   Ansys Inc, Theory Guide and User's Guide **2015**.

[36]   MATLAB Inc, Numerical computing with MATLAB. *Choice Rev. Online* **2005**.

[37]   J. F. Thompson, B. K. Soni, N. P. Weatherill, *Handbook of Grid Generation*, Taylor & F., **1998**.

[38]   B. W. Righolt, S. Kenjereš, R. Kalter, M. J. Tummers, C. R. Kleijn, *Int. J. Heat Fluid Flow* **2016**, *62*, 395.

[39]   N. J. Lawson, M. R. Davidson, *J. Fluids Struct.* **2001**, *15*, 59.

[40]   A. Maurel, P. Ern, B. J. A. Zielinska, J. E. Wesfreid, *Phys. Rev. E* **1996**, *54*, 3643.

[41]   P. J. W. Roberts, D. R. Webster, "Environmental fluid mechanics: Theories and applications," *Turbulent diffusion in environmental fluid mechanics theories and application*, S. Hayley, A. Cheng,

W. Keh-han, M. Teng, L. Clark, Eds., ASCE publishers, Reston, USA **2002**, Vol. 90, p. 7.

[42]   X. Yao, Y. Zhang, L. Du, J. Liu, J. Yao, *Renew. Sustain. Energy Rev.* **2015**, *47*, 519.

[43]   A. Lee, G. H. Yeoh, V. Timchenko, J. A. Reizes, *Appl. Therm. Eng.* **2012**, *48*, 275.

[44]   A. Dumas, M. Subhash, M. Trancossi, J. P. Marques, *Energy Procedia* **2014**, *45*, 626.

[45]   N. S. Hasabnis, K. A. Totlani, V. V. Ranade, *Can. J. Chem. Eng.* **2015**, *93*, 1860.

[46]   R. K. Shah, A. L. London, "Circular Duct," *Laminar Flow Forced Convection in Ducts*, Elsevier **1978**, Vol. 16, p. 78.

[47]   S. Haase, D. Y. Murzin, T. Salmi, *Chem. Eng. Res. Des.* **2016**, *113*, 304.

[48]   P. V. Danckwerts, *Chem. Eng. Sci.* **1953**, *2*, 1.

[49]   J. Sierra-Pallares, T. Huddle, E. Alonso, F. A. Mato, J. García-Serna, M. J. Cocero, E. Lester, *Chem. Eng. J.* **2016**, *299*, 373.

[50]   M. T. Kreutzer, F. Kapteijn, J. A. Moulijn, J. J. Heiszwolf, *Chem. Eng. Sci.* **2005**, *60*, 5895.

[51]   X. Ni, M. R. Mackley, A. P. Harvey, P. Stonestreet, M. H. I. Baird, N. V. Rama Rao, *Chem. Eng. Res. Des.* **2003**, *81*, 373.

[52]   K. Madane, A. A. Kulkarni, *Chem. Eng. Sci.* **2018**, *176*, 96.

[53]   L. Siconolfi, A. Fani, S. Camarri, M. V. Salvetti, *Eur. J. Mech. - B/Fluids* **2016**, *55*, 360.

[54]   S. R. L. Gobert, S. Kuhn, L. Braeken, L. C. J. Thomassen, *Org. Process Res. Dev.* **2017**, *21*, 531.